

ONE HUNDRED FIRST STARS : PROTOSTELLAR EVOLUTION AND THE FINAL MASSES

SHINGO HIRANO¹, TAKASHI HOSOKAWA², NAOKI YOSHIDA^{3,4}, HIDEYUKI UMEDA¹,
KAZUYUKI OMUKAI⁵, GEN CHIAKI³, AND HAROLD W. YORKE⁶

Draft version August 7, 2018

ABSTRACT

We perform a large set of radiation hydrodynamics simulations of primordial star formation in a fully cosmological context. ^a Our statistical sample of *100 First Stars* show that the first generation of stars have a wide mass distribution $M_{\text{popIII}} = 10 \sim 1000 M_{\odot}$. We first run cosmological simulations to generate a set of primordial star-forming gas clouds. We then follow protostar formation in each gas cloud and the subsequent protostellar evolution until the gas mass accretion onto the protostar is halted by stellar radiative feedback. The accretion rates differ significantly among the primordial gas clouds which largely determine the final stellar masses. For low accretion rates the growth of a protostar is self-regulated by radiative feedback effects and the final mass is limited to several tens of solar masses. At high accretion rates the protostar's outer envelope continues to expand and the effective surface temperature remains low; such protostars do not exert strong radiative feedback and can grow in excess to one hundred solar masses. The obtained wide mass range suggests that the first stars play a variety of roles in the early universe, by triggering both core-collapse supernovae and pair-instability supernovae as well as by leaving stellar mass black holes. We find certain correlations between the final stellar mass and the physical properties of the star-forming cloud. These correlations can be used to estimate the mass of the first star from the properties of the parent cloud or of the host halo, without following the detailed protostellar evolution.

Subject headings: stars: Population III – early universe – stars: evolution – stars: formation – accretion, accretion disks – stars: pre-main sequence

1. INTRODUCTION

The first stars played a key role in the early universe. Their first light initiated cosmic reionization, and the heavy elements synthesized by them enabled the formation of subsequent ordinary stellar populations (e.g., Alvarez et al. 2006; Johnson et al. 2007; Maio et al. 2011; Wise et al. 2012; Karlsson et al. 2013). The first stars could have also seeded the formation of supermassive black holes observed at high redshifts (Li et al. 2007; Volonteri 2012; Hosokawa et al. 2012a, 2013). Understanding the formation of the first stars is thus necessary to understand the early history of the universe (e.g., Bromm et al. 2009). Theoretical studies are rapidly advancing our knowledge on how the first stars are formed from the cosmic primordial gas, supplemented by a variety of observations ranging from Galactic metal-poor stars to high redshift galaxies that provide invaluable information on early star formation (Bromm & Yoshida 2011). However, there still remain an important question on the nature of the first generation of stars: *what is the characteristic mass distribution*

of the first stars? The fate of a star and the strength of various stellar feedback effects on the local environment are largely determined by the star's mass, and it is thus crucial to know the characteristic mass of the first stars.

The initial conditions of the first stars' formation are determined cosmologically; small density perturbations left over from the Big Bang drive, via gravitational instability, the formation of primordial star-forming gas clouds. It has become possible to perform *ab initio* numerical simulations to follow this process (e.g., Abel et al. 2002; Yoshida et al. 2008; Greif et al. 2012). Such cosmological simulations show that small dark matter halos ($\sim 10^5 - 10^6 M_{\odot}$) forming at redshift $z \sim 20 - 30$ are cradles of the first stars (e.g., Yoshida et al. 2003; Gao et al. 2007; O'Shea & Norman 2007). Typically, a massive star-forming gas cloud of $\sim 1000 M_{\odot}$, which is gravitationally unstable, is formed at the density peak of the host dark matter halo. The cloud gravitationally collapses with help of radiative cooling by hydrogen molecules (e.g., Matsuda et al. 1969; Palla et al. 1983). The collapse continues until a quasi-hydrostatic protostellar core ($\sim 0.01 M_{\odot}$) is formed in the densest part of the cloud (e.g., Omukai & Nishi 1998; Yoshida et al. 2008).

There is still a long way for this protostar to grow in mass and ultimately reach the Pop III main-sequence. The initially tiny protostellar core grows via accretion of the surrounding gas. The typical accretion rate in a primordial gas cloud is $10^{-3} - 10^{-2} M_{\odot} \text{ yr}^{-1}$, with which most of the gas in the cloud can be accreted onto the star during its stellar lifetime ($\sim \text{Myr}$). It has been postulated that the final stellar mass is set by the mass of the natal cloud, which is as massive as $M_{\text{cloud}} \sim 100 - 1000 M_{\odot}$. This is too naive an estimate, however. The

¹ Department of Astronomy, School of Science, University of Tokyo, Bunkyo, Tokyo 113-0033, Japan

² Department of Physics and Research Center for the Early Universe, University of Tokyo, Bunkyo, Tokyo 113-0033, Japan

³ Department of Physics, School of Science, University of Tokyo, Bunkyo, Tokyo 113-0033, Japan

⁴ Kavli Institute for the Physics and Mathematics of the Universe (WPI), Todai Institutes for Advanced Study, the University of Tokyo, Kashiwa, Chiba 277-8583, Japan

⁵ Astronomical Institute, Tohoku University, Sendai, Miyagi 980-8578, Japan

⁶ Jet Propulsion Laboratory, California Institute of Technology, Pasadena CA 91109, USA

^a ©2013: All rights reserved

final stellar mass is determined by a complex interplay between the growing central protostar and the accreting gas. Radiation from the protostar critically affects the process and possibly halts gas accretion hence its mass growth (Hosokawa et al. 2011, 2012b).

The strength of the UV radiative feedback depends on the stellar luminosity and effective temperature, which are determined by the evolution of the protostar itself. The structure and evolution of an accreting primordial protostar have been studied in detail by numerically solving the interior structure (e.g., Stahler et al. 1986; Omukai & Palla 2001, 2003; Ohkubo et al. 2009; Hosokawa et al. 2012a). McKee & Tan (2008) develop an analytic model of the protostar’s evolution and apply it to a particular case to find the final stellar mass to be around $140 M_{\odot}$.

Numerical simulations are necessary to follow the growth of the protostar and the detailed interplay between the star and the surrounding gas self-consistently, because the UV feedback influences directly and almost instantaneously the mass accretion rate. The first such simulations of Hosokawa et al. (2011) show that the UV radiative feedback is strong enough to halt gas accretion when the stellar mass is around a few tens of solar masses (see also Stacy et al. 2012; Susa 2013).

Observationally, the typical mass of the first stars can be inferred, for example, from the elemental abundance patterns of metal-poor stars in the Galaxy (Caffau et al. 2011). Interestingly, the abundance patterns found in the atmospheres of a few extremely metal-poor stars can be reconciled, if the metals are produced in supernovae of progenitor stars with a mass $\leq 100 M_{\odot}$ (Umeda & Nomoto 2005). This relative small mass is consistent with the conclusion of recent theoretical studies on primordial star formation (Hosokawa et al. 2011). Very massive stars with $150 - 300 M_{\odot}$ end their lives as pair-instability supernovae (PISNe; Barkat et al. 1967; Bond et al. 1984; Heger & Woosley 2002). PISNe would imprint a peculiar abundance pattern in metal-poor stars, a pattern for which there is no clear observational indication (Tumlinson et al. 2004; Frebel et al. 2009).

Previous theoretical studies examine only a limited number of cases to derive the final stellar masses. The characteristic mass and the overall mass distribution are yet unknown. A large set of simulations beginning from the earliest phases of structure formation in the universe are needed to derive the mass distribution of the first stars.

In this paper we study the statistical properties of the first stars, using more than one hundred clouds produced in a cosmological simulation. To this end, we first run a large-volume cosmological simulation which follows the formation of primordial clouds in dark matter halos and their initial run-away collapse (Yoshida et al. 2006, 2008; Hirano & Yoshida 2013). We then switch to the radiation hydrodynamic simulations coupled with stellar evolution calculations, which follow the subsequent evolution in the accretion phase until the mass accretion onto the protostar is shut off by strong stellar UV feedback (Hosokawa et al. 2011, 2012b). From these simulations we obtain a distribution of stellar masses, which, as we find, ranges from just under ten to more than one thousand solar masses.

The rest of the paper is organized as follows. In Section

2, we briefly describe the numerical methods employed in our cosmological simulation, the radiation hydrodynamic simulations, and the stellar evolution calculations. Section 3 presents the results of our *100 First Stars* simulations; statistical variations regarding the first stars’ formation and the resulting distribution of stellar masses. In Section 4, we investigate the origins of the wide distribution of the final stellar masses. Section 5 and 6 provide the relevant discussions and concluding remarks of this study.

2. METHODS

We first perform cosmological N -body SPH (Smoothed-Particle-Hydrodynamics) simulations of early structure formation. We locate and label dense and cold gas clumps hosted by small mass dark halos as sites for primordial star formation. We follow the pre-stellar collapse of each cloud up to the formation of a protostar. We then switch to two dimensional axisymmetric radiation hydrodynamics simulations of protostellar evolution that start with the output of our cosmological simulations. The following subsections describe our numerical methods. We highlight several novel techniques that are introduced for the present study.

2.1. Cosmological Simulations: Primordial Gas Clouds

Our Λ -Cold Dark Matter (Λ CDM) simulations adopt the cosmological parameters consistent with the WMAP 9-year data Komatsu et al. (2011). The basic simulation parameters are summarized in Table 1. All the cosmological simulations are initialized at $z_{\text{ini}} = 99$.

We use the parallel N -body / SPH solver *GADGET-2* (Springel 2005) in its version suitably adopted for primordial star formation as in Hirano & Yoshida (2013). We solve chemical rate equations for 14 primordial species (e^{-} , H, H^{+} , H^{-} , He, He^{+} , He^{++} , H_2 , H_2^{+} , D, D^{+} , HD, HD^{+} , HD^{-}) as in Yoshida et al. (2006, 2007). To accurately evaluate trapping effects of cooling radiation, we employ the Sobolev method for H_2 line cooling and a ray-tracing method for continuum cooling by H_2 collision-induced emission (Hirano & Yoshida 2013).

The main parent simulations have a sufficiently large volume of $L_{\text{box}} = 1$ and $2 \text{ h}^{-1} \text{ Mpc}$ on a side. We also use a few additional simulations with smaller volumes. There are a number of primordial clouds at redshifts $10 - 30$. The typical mass of the star-forming clouds, $\sim 1000 M_{\odot}$, is resolved with more than 128 SPH particles. We employ a hierarchical zoom-in re-simulation method to resolve a primordial gas cloud with a progressively larger number of particles. Each refined region has a spherical shape of radius $130 \text{ h}^{-1} \text{ kpc}$ in the case of $L_{\text{box}} = 1 \text{ h}^{-1} \text{ Mpc}$. All the re-simulations are started from $z = 99$.

We run a friends-of-friends halo finder to locate dense, clustered regions in the parent cosmological simulations. Then we generate the initial conditions for the selected regions, where the mass- and spatial-resolution are increased. The corresponding small-scale density fluctuations are added suitably as given by our adopted Λ CDM cosmology. The selection of the gas clouds is done as follows. First, we select a virialized dark matter halo whose mean density within the virial radius is 200 times greater than the mean density of the universe, i.e., $n_{\text{dm}} > n_{\text{vir}} \sim 200 n_{\text{univ}}$. Then, if the halo is the

TABLE 1
PARAMETERS OF COSMOLOGICAL SIMULATIONS

N_{sample}	L_{box} (h^{-1} kpc)	N_{zoom}	$l_{\text{soft, zoom}}$ (h^{-1} pc)	$m_{\text{DM, zoom}}$ ($h^{-1} M_{\odot}$)	$m_{\text{Gas, zoom}}$ ($h^{-1} M_{\odot}$)	
3	50	1024	1.0	0.0142	0.00288	(1)
3	150	2048	1.5	0.0478	0.00971	(1)
1	300	2048	2.9	0.383	0.0772	(1)
7	1000	3072	6.5	2.16	0.436	(2)
75	1000	1536	13.5	17.3	3.49	(3)
21	2000	3072	13.5	17.3	3.49	(2)

NOTE. — Column 1: Number of star-forming clouds, Column 2: Simulation box size (comoving), Column 3: The effective grid resolution in the zoomed region, Column 4: Gravitational softening length (comoving), Column 5: Dark matter particle mass, Column 6: Gas particle mass, and Column 7: Reference of the adopted cosmological parameters.

REFERENCES. — (1) Larson et al. 2011; (2) Komatsu et al. 2009; (3) Komatsu et al. 2011.

densest structure within a 2 physical kpc radius around itself, we assume the halo has not been influenced by supernova explosions of nearby stars (e.g., Ritter et al. 2012) nor by radiative feedback (e.g., O’Shea & Norman 2008; Agarwal et al. 2012; Johnson et al. 2013). Primordial gas clouds forming at the centers of such halos are thought to bear the first generation of stars. In this way, we locate and select a sample of 110 gas clouds from the parent cosmological simulations.

Our zoom-in simulations follow the formation and gravitational run-away collapse of the selected primordial gas clouds. We use the particle-splitting technique of Kitsionas & Whitworth (2002) to achieve a wide dynamic range. By this method, the local Jeans length is always resolved by 10 times the local smoothing length of the SPH particles. We stop our zoom-in simulations when the central density of the cloud reaches $n_{\text{H, cen}} = 10^{13} \text{ cm}^{-3}$. At this moment, the mass of the lightest gas particle is $m_{\text{gas}} \sim 10^{-5} M_{\odot}$, and thus the nominal mass resolution is $\sim 0.01 M_{\odot}$. The model outputs at this time are used to generate the *initial* conditions for our protostellar evolution calculations.

2.2. Radiation Hydrodynamic Simulations: Evolution of Accreting Protostars

We follow the evolution of the protostars in the accretion phase using 2D axisymmetric radiation hydrodynamic (RHD) calculations coupled with the stellar structure evolution (Hosokawa et al. 2011). The nested-grid method (e.g., Yorke & Kaisig 1995; Yorke & Bodenheimer 1999; Yorke & Sonnhalter 2002) is employed in order to achieve an extremely wide dynamic range. Our calculations utilize 9 level hierarchical grids, whereby the coarsest grid size is ~ 6400 AU and the finest is ~ 25 AU in a ~ 1 pc volume. Data from the three-dimensional cosmological simulation are mapped onto two-dimensional axisymmetric meshes as follows. First, we fix the principal rotational axis by calculating the average angular momentum vector of the gas within a 0.01 pc region around the cloud center. Then we take averages of physical quantities along the azimuthal direction around the rotational axis under the 8 level hierarchical grids. The free flow boundary conditions are adopted in the RHD simulations; the material can escape and enter through the edges of the simulation domains. We assume that the density at the boundary is the same as that of the outermost grid. To eliminate the effects of this boundary condition, we set a sufficiently large box

size so that the inflow cannot affect the accretion onto the central protostar. The computational domain is 1.2 pc on a side, which typically contains a few thousands solar masses of gas.

We consistently follow the structure and evolution of the central accreting star and the hydrodynamics of the accreting gas which is irradiated by the stellar radiation as in Hosokawa et al. (2011). The mass accretion rate onto the protostar is directly obtained from the inflow rate of gas into the central sink cell in the RHD simulation. Our code treats non-equilibrium chemistry and radiative processes in a primordial gas (summary of the reactions are found in Hosokawa et al. 2011). We have verified that HD cooling, which sometimes operates in the pre-collapse stage (see Sec. 3.2.2 below), is unimportant in the vicinity of the protostar and in the accretion disk. We switch off the HD chemistry in our protostellar evolution calculations (Hosokawa et al. 2012b).

The evolution of the protostar is calculated by numerically solving the interior structure with this accretion rate (e.g., Omukai & Palla 2003; Hosokawa & Omukai 2009). The stellar luminosity and the effective temperature are provided by the stellar model. The spectral energy distribution is calculated from these basic properties of the star.

We explore various cases with different gas accretion rates and different protostellar evolution. To this end, we have added several modifications to the code used in Hosokawa et al. (2011, 2012b). The improvements are summarized as follows (see also Appendixes A and B).

- Angular momentum transport in a rapidly accreting circumstellar disk is driven mainly by its non-axisymmetric structures such as spiral arms. Hosokawa et al. (2011) adopt the so-called α -viscosity model (Shakura & Sunyaev 1973) using a constant gravo-viscous parameter α everywhere on the equator of the disk (e.g., Yorke & Sonnhalter 2002). Recent 3D numerical simulations suggest that, in a self-gravitating disk, the effective α can be estimated as a function of the Toomre Q -parameter (Zhu et al. 2010b; Takahashi et al. 2013). Motivated by this, we adopt a functional form proposed by Gammie (1996), and allow α to spatially vary with the Toomre Q -parameter evaluated at each cell on the equator, $\alpha(Q(r))$. Details of this procedure are described in Appendix A.
- In a number of our cases we find rather high ac-

cretion rates, exceeding $0.01 M_{\odot} \text{ yr}^{-1}$ (Sec. 3.3 below). For sufficiently high accretion rates, the protostellar evolution differs significantly from the fiducial case, whereby the star contracts to reach the zero-age main-sequence (Omukai & Palla 2003; Hosokawa et al. 2012a, also see Sec. 2.2.1). In practice, we occasionally encounter convergence difficulties with time-dependent accretion histories resulting from our RHD simulations. We avoid this technical problem by employing an analytic model of stellar evolution. In essence, we assume that the rapidly accreting star, whose envelope experiences expansion and oscillations, nevertheless evolves on a certain averaged track on the mass-radius plane. We describe the details of our analytic model in Appendix B.

We assume that the mass accretion and hence the growth of the central star are halted due to stellar radiative feedback, when the mass accretion rate falls below $10^{-4} M_{\odot} \text{ yr}^{-1}$. We stop the calculation at this time. In fact Hosokawa et al. (2011, 2012a) show that the accretion rate continues to decrease after that and further stellar growth in mass is negligible. The final stellar mass generated by each of the 110 collapsing clouds represent a statistical sample of the final masses of the first stars, M_{popIII} .

2.2.1. Three Paths of the Protostellar Evolution

It is known that an accreting protostar goes through a qualitatively different evolution depending on the accretion rate (e.g., Omukai & Palla 2003; Hosokawa et al. 2012a). We classify the notably different protostellar evolutionary paths into three characteristic cases. For completeness we first review briefly each evolutionary path, in order to better describe our main results presented in the following sections. In the figures hereafter, the three evolutionary paths are distinguished by using different colors (red, blue, and black) for clarity.

KH Contracting Protostar (P1; $\dot{M} < 4 \times 10^{-3} M_{\odot} \text{ yr}^{-1}$)—

The evolution of an accreting protostar is approximately determined by the balance between the following two physical timescales. One is the stellar Kelvin-Helmholtz (KH) timescale, over which the protostar radiates away its gravitational energy,

$$t_{\text{KH}} \equiv \frac{GM_{\text{star}}^2}{R_{\text{star}}L_{\text{star}}}, \quad (1)$$

where M_{star} , R_{star} , and L_{star} are the stellar mass, radius, and luminosity, respectively. This is an approximate timescale for a non-accreting protostar to contract to the main-sequence. The other is the accretion timescale, over which the protostar doubles its mass by accretion,

$$t_{\text{acc}} \equiv \frac{M_{\text{star}}}{\dot{M}}, \quad (2)$$

where \dot{M} is the mass accretion rate.

In Figure 1, the case with $\dot{M} = 10^{-3} M_{\odot} \text{ yr}^{-1}$ corresponds to the evolution of the KH contracting protostar. In an early evolutionary stage when $M_{\text{star}} \leq 5 M_{\odot}$, the KH timescale is longer than the accretion timescale, $t_{\text{KH}} \gg t_{\text{acc}}$, so that the energy deposition by accretion

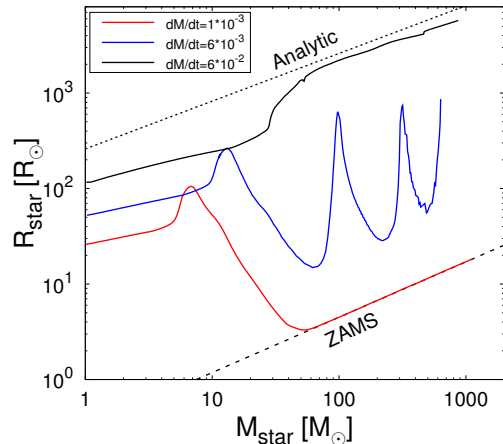


FIG. 1.— Evolution of the accreting protostar’s radius for three constant accretion rates $\dot{M} = 1 \times 10^{-3}$, 6×10^{-3} , and $6 \times 10^{-2} M_{\odot} \text{ yr}^{-1}$ (taken from Hosokawa et al. 2012a). The dotted and dashed lines represent the mass-radius relations for super-giant protostars (Eq. 7) and ZAMS stars.

is faster than the energy loss by radiation (this is called “adiabatic accretion”; Stahler et al. 1986). When M_{star} exceeds $5 M_{\odot}$ the stellar luminosity begins to increase sharply, and the KH timescale quickly decreases with increasing stellar mass. The KH timescale eventually falls below the accretion timescale, and the protostar is able to efficiently radiate away its internal energy; it begins to contract ($M_{\text{star}} \geq 7 M_{\odot}$; “KH contraction”). KH contraction continues until the star begins core hydrogen burning at $M_{\text{star}} \simeq 40 M_{\odot}$, a point at which it has essentially reached the zero-age main-sequence (ZAMS).

Oscillating Protostar (P2; $\dot{M} > 4 \times 10^{-3} M_{\odot} \text{ yr}^{-1}$)—

Omukai & Palla (2003) show that, with rapid mass accretion, the star begins expanding before reaching the ZAMS. Figure 1 illustrates this for the case $\dot{M} = 6 \times 10^{-3} M_{\odot} \text{ yr}^{-1}$. Abrupt expansion occurs when the stellar total luminosity approaches the Eddington value during KH contraction. The critical accretion rate above which this abrupt expansion occurs has been studied by Omukai & Palla (2003). The total luminosity at the accreting envelope

$$L_{\text{env}} = L_{\text{star}} + L_{\text{acc}} \simeq L_{\text{star}} + \frac{GM_{\text{star}}\dot{M}}{R_{\text{star}}} \quad (3)$$

becomes equal to the Eddington luminosity L_{Edd} when the star reaches the ZAMS. The condition for the critical value is thus $L_{\text{env}}|_{\text{ZAMS}} = L_{\text{ZAMS}} + L_{\text{acc,ZAMS}} = L_{\text{Edd}}$, from which we obtain

$$L_{\text{Edd}} = L_{\text{ZAMS}} + \frac{GM_{\text{ZAMS}}\dot{M}_{\text{P2}}}{R_{\text{ZAMS}}}, \quad (4)$$

$$\begin{aligned} \dot{M}_{\text{P2}} &= \frac{R_{\text{ZAMS}}}{GM_{\text{ZAMS}}}(L_{\text{Edd}} - L_{\text{ZAMS}}) \\ &\approx 4 \times 10^{-3} M_{\odot} \text{ yr}^{-1}. \end{aligned} \quad (5)$$

Note that \dot{M}_{P2} given by this equation is a function of M_{star} , but its dependence is weak (Omukai & Palla

2003). If the mass accretion rate is higher than this critical value during KH contraction, $\dot{M} > \dot{M}_{P2}$, the star’s total luminosity approaches the Eddington value before arriving at the ZAMS. The star can not contract any more and begins to expand. This *bloating* results from the high specific entropy gain in surface layers, where the opacity is higher than the interior, as they absorb a part of the outward heat flux. However, only these surface layers begin to inflate; the bulk of the stellar mass continues KH contraction (see below). As the star inflates, the Eddington ratio ($L_{\text{tot}}/L_{\text{Edd}}$) decreases with decreasing accretion luminosity. After reaching a significantly lower Eddington ratio the star resumes KH contraction, thereby completing one cycle of oscillation. The oscillatory timescale in this evolutionary stage is approximately given by the KH timescale, the thermal adjustment timescale of the star.

Super-Giant Protostar (P3; $\dot{M} > 4 \times 10^{-2} M_{\odot} \text{ yr}^{-1}$)—

Hosokawa et al. (2012a) show that, if the accretion rate is higher than

$$\dot{M}_{P3} \approx 4 \times 10^{-2} M_{\odot} \text{ yr}^{-1}, \quad (6)$$

the protostar enters a third evolutionary path, whereby the stellar radius monotonically increases with stellar mass according to the relation

$$R_{\text{star}} \simeq 2.6 \times 10^2 R_{\odot} \left(\frac{M_{\text{star}}}{M_{\odot}} \right)^{1/2} \quad (7)$$

for $M_{\text{star}} > 100 M_{\odot}$. The above scaling is independent of the mass accretion rate as long as it is greater than the critical value, \dot{M}_{P3} . In Figure 1, the case with $6 \times 10^{-2} M_{\odot} \text{ yr}^{-1}$ demonstrates this behavior. Note that, even in this case, the timescale inversion to $t_{\text{KH}} < t_{\text{acc}}$ occurs at $M_{\text{star}} \simeq 30 M_{\odot}$. This means that most of the stellar interior contracts, radiating the energy away and only a surface layer significantly inflates. The star thus has a highly inhomogeneous structure, whereby the contracting core is surrounded by a bloating envelope, similar to red-giant stars. This evolutionary path is appropriately called the “super-giant protostar” (Hosokawa et al. 2012a).

Hosokawa et al. (2012a) calculate the protostar evolution with large constant accretion rates, with which the protostar evolves on the “super-giant” track. In the present paper, we use varying mass accretion which is self-consistently calculated. We find that protostars begin to contract when the accretion rates become sufficiently low.

3. RESULTS

3.1. Overview

The results presented here are based on a sequence of simulations with different computer codes. We first perform SPH cosmological simulations to follow the formation of the primordial gas clouds which gravitationally collapse in the center of dark matter halos. The histogram in Figure 2 shows that our sample of 110 dark matter halos have a wide range of masses $M_{\text{virial}} = 10^5 - 10^6 M_{\odot}$ distributed over redshifts $z = 35 - 11$, most of which are at $z = 20 - 15$. Figure 3 shows an example of the resulting gas density concentrations arising in five such dark matter halos together with insets

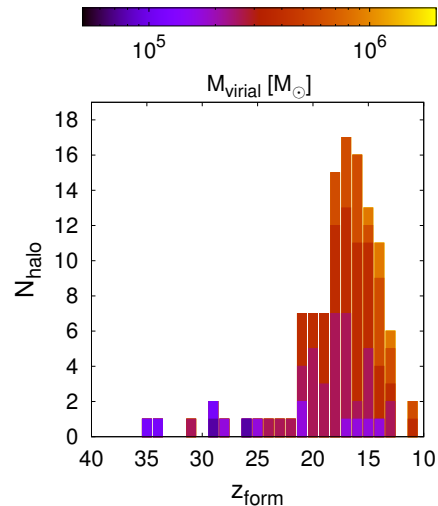


FIG. 2.— The number of dark matter halos that host star-forming gas clouds. The histogram shows the distribution of redshifts when the central gas density reaches $\sim 10^6 \text{ cm}^{-3}$. The histograms are colored according to the virial masses using the color scale displayed at the top.

TABLE 2
EVOLUTIONARY PATHS

Path	\dot{M} ($M_{\odot} \text{ yr}^{-1}$)	N_{sample}
P1 KH Contracting Protostar	< 0.004	67
P2 Oscillating Protostar	$> 0.004^1$	31
P3 Super-Giant Protostar	$> 0.04^2$	12

NOTE. — Column 2: Accretion rate for each path, and Column 3: The number of stars in our sample.

REFERENCES. — (1) Omukai & Palla 2003; (2) Hosokawa et al. 2012.

of their zoomed-in structure, represented by white circles corresponding to 1 pc. As expected, the five clouds have different structures of density, velocity, and temperature. The resulting stellar masses are also different as indicated in the figure.

After the formation of a protostellar core at the center of the collapsing cloud, we switch to the 2D RHD calculations for each individual dark matter halo and follow the evolution during the later accretion stages. Figure 4 shows snapshots from three of our examined cases, which exemplify the three different evolutionary paths (P1, P2, and P3). We see that in each case a bipolar HII region forms (Figure 4a), which subsequently grows at varying rates as the stellar mass increases. The mass accretion onto the protostar is finally shut off by the strong UV radiative feedback caused by the dynamical expansion of the HII region (Figure 4c; see also Hosokawa et al. 2011). Figure 5 shows the distribution of the final stellar masses obtained in our simulations (a summary is given in Table 2). We see a large scatter of resulting stellar masses, ranging from $9.9 M_{\odot}$ to $1621 M_{\odot}$. However, the bulk of them is distributed around several tens or a few hundreds of solar masses. We study the origin of this distribution in Sec. 4 in detail. Here, we merely note that the distribution of stellar masses does not mirror the distribution

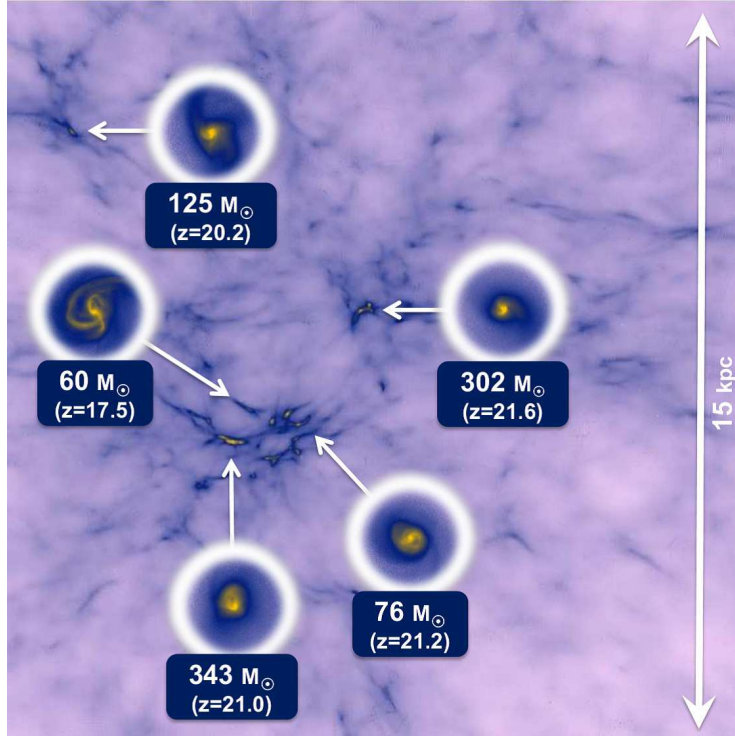


FIG. 3.— Projected gas density distribution at $z = 25$ in one of our cosmological simulations. We show five primordial star-forming clouds in a cube of 15 kpc on a side. The circles show the zoom-in to the central 1 pc region of the clouds at the respective formation epoch. The masses of the first stars formed in these clouds are 60, 76, 125, 303, and 343 M_{\odot} , respectively.

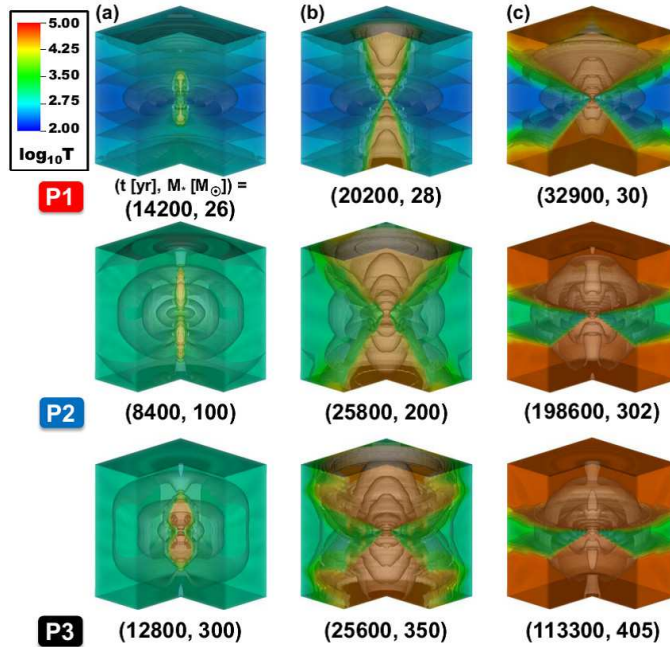


FIG. 4.— Expanding HII regions around the primordial protostar for three in our sample of 110 clouds (the same ones as in Figure 12). We show the structure and the evolution of the accreting gas from left to right. The plotted regions are cubes with 60000 AU on a side. The colors indicate gas temperature and the contours show the density structure. The main accretion takes place through the accretion disk on the equatorial plane. As the central protostar becomes more massive and the surface temperature increases, the ionizing photon production of the central star increases. HII regions are launched into the polar direction and the opening angles grow with time, eventually stopping the accretion.

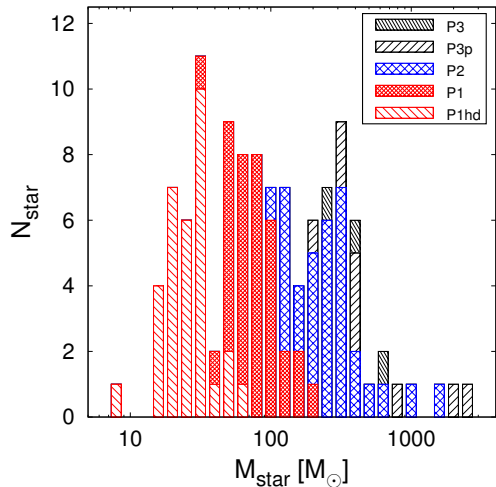


FIG. 5.— The final distribution of the calculated stellar masses for our 110 first stars. The red, blue, and black histograms represent the different paths of protostellar evolution; P1: KH contracting protostar (red), P2: oscillating protostar (blue), and P3: super-giant protostar (black). See text in Sec. 2.2.1 for details. P1hd refers to the cases in which the gas clouds are formed by HD cooling and evolve on low-temperature tracks. P3p (predicted) indicates the same cases as P3, except that the final masses are calculated from a correlation between the properties of the cloud and the resulting stellar mass (Eq. 13; see Appendix B).

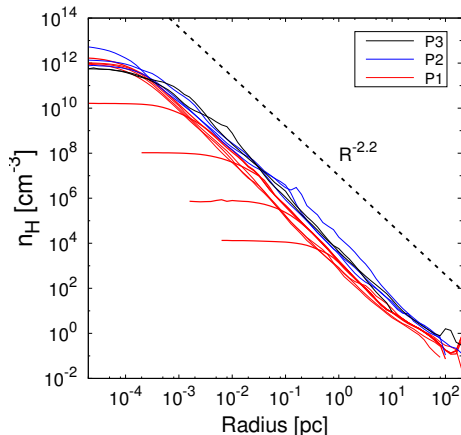


FIG. 6.— Radial gas density profiles for 9 selected star-forming clouds. The colors indicate the different stellar evolutionary paths P1 (red, 4 cases), P2 (blue, 3 cases), and P3 (black, 2 cases). For one P1 case we also plot the time evolution of the density profile at the time when the central density is 10^4 , 10^6 , 10^8 , 10^{10} , and 10^{12} cm^{-3} . For all other clouds, we use snapshots at $n_{\text{H,cen}} \simeq 10^{12}$ cm^{-3} . The black dotted line shows a power-law density distribution with $n_{\text{H}} \propto R^{-2.2}$ for reference.

of dark matter halo masses.

3.2. Evolution in the Early Collapse Stage

3.2.1. Run-away Collapse of the Clouds

In this section we describe the early evolution of the star-forming clouds up to the moment when a central hydrostatic core is formed by considering the fate of nine representative cases. Figure 6 shows that the gravitational collapse of a primordial cloud proceeds in the well-known self-similar manner. The cloud has a central collapsing core and a surrounding envelope during

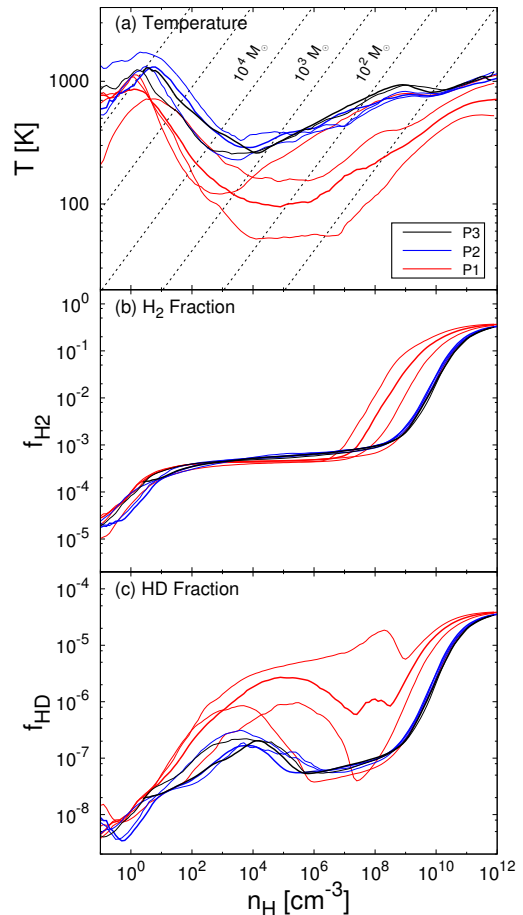


FIG. 7.— Gas temperature (*top panel*), H_2 fraction (*middle*), and HD fraction (*bottom*) distributions as a function of gas number density, n_{H} , for the same 9 clouds in Fig. 6 when the central (highest) density is $n_{\text{H,cen}} = 10^{12}$ cm^{-3} . We calculate the mass-weighted mean values of the gas SPH particles for each density bin. The dashed lines show the $n_{\text{H}} - T$ relation for the given Jeans masses.

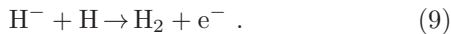
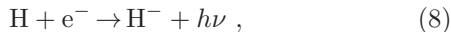
the collapse. Whereas the collapsing core has an approximately homogeneous density distribution, the envelope develops a power-law distribution, $n_{\text{H}} \propto R^{-2.2}$ (e.g., Omukai & Nishi 1998; Ripamonti et al. 2002). Figure 6 also shows the radially-averaged density profiles in the nine different clouds at the time when the central density reaches 10^{12} cm^{-3} . We see that densities at the same radial distance can differ among the clouds by more than a factor of ten. The variation of the density structure is attributed to the different thermal evolution during the collapse (see Sec. 3.2.2 below). Some bumps in the density profiles indicate the presence of neighboring density peaks, large disk- or bar-like structure, and/or fragmenting clumps in the collapsing clouds. We discuss these cases further in Sec. 5.2.2.

3.2.2. Thermal Evolution During the Collapse

Next, we address the thermal evolution of the collapsing primordial star-forming clouds. We show the distributions of the temperature and density in the envelope

when the central density is $\simeq 10^{12} \text{ cm}^{-3}$ (Figures 6 and 7). The $n - T$ profiles in the envelope at a particular time essentially trace the thermal evolution of the contracting core due to the self-similar nature of the collapse.

The thermal evolution of a collapsing cloud is largely determined by non-equilibrium cooling and heating processes. The most important coolant of the primordial gas is molecular hydrogen H_2 . Figures 7(a) and (b) show that the cloud is heated up to $\sim 1000 \text{ K}$ due to virialization at $n_{\text{H}} < 10^2 \text{ cm}^{-3}$, as the H_2 fraction slowly increases via the two-body reaction,



When a sufficient amount of H_2 is formed, the gas temperature begins to decrease to $100 - 200 \text{ K}$ due to H_2 line cooling.

Figure 7(a) shows that, in several cases, the gas temperature becomes lower than 200 K , which is unexpectedly low for the so-called Pop III.1 star formation scenario (Bromm et al. 2009). The low temperature tracks are more similar to that expected from Pop III.2 star formation where HD molecular cooling operates. Indeed, Figure 7(c) shows that HD molecules are efficiently formed in these cases, suggesting that the low temperatures are due to HD line cooling. HD cooling is usually negligible for Pop III.1 star formation (Ripamonti 2007). In the Pop III.2 star formation scenario H_2 formation is enhanced if the initial electron abundance is high (see Eqs. 8 and 9). As a result, the temperature becomes low enough to form HD molecules, and even drops below 100 K with the additional HD molecular cooling. This is not the explanation in our cases, however, since we do not see a significant enhancement of the electron abundance.

Interestingly, the timescale of cloud collapse plays an important role in determining the thermal evolution. Although the collapse timescale is always comparable to the free-fall timescale for an average given density, the collapse can be decelerated, e.g., by rotational support if the cloud has finite angular momentum. When the collapse is slower, more H_2 molecules are produced via reactions (8) and (9). With the enhanced radiative cooling from the more abundant H_2 , the temperature becomes sufficiently low to allow HD formation and cooling. Note that the slight difference in molecular binding energy triggers chemical fractionation at low temperatures. Once HD molecular line cooling begins to operate, the temperature decreases further down to a few tens of Kelvin. In one extreme case, the temperature attains the floor of the cosmic microwave background (CMB), $T_{\text{CMB}} = 2.73 (1 + z) \simeq 50 \text{ K}$ at $z \simeq 20$. Thus, we conclude that the effects of a slow collapse are indeed significant. When the collapse time is only a few times longer than the free-fall time, the resulting thermal evolution becomes similar to that of the Pop III.2 case driven by HD cooling. We have also confirmed this behavior by using one-zone models for following the thermal evolution during the cloud collapse (e.g., Omukai 2000). Our detailed analysis is described in Appendix C.

HD cooling becomes inefficient at densities greater than 10^8 cm^{-3} . However, the abundance of H_2 molecules

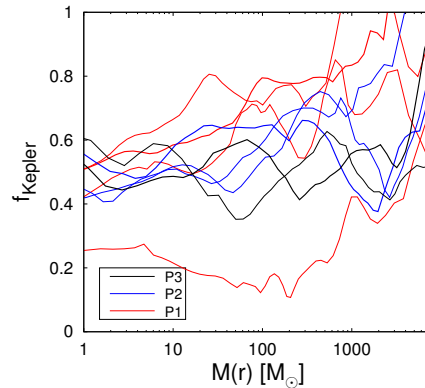


FIG. 8.— Averaged profiles of the degree of rotational support, $f_{\text{Kepler}} = v_{\text{rot}}/v_{\text{Kepler}}$, for the same 9 clouds in Fig. 6 at the moment when $n_{\text{H, cen}} = 10^{12} \text{ cm}^{-3}$. The lowest line represents the case for which the cloud is most slowly rotating in our sample (see Figure 18a and Table 4). Generally, f_{Kepler} is large for P1, P2, and P3 in this order.

begins to increase as the so-called three-body formation process,



comes into play, which converts nearly all the hydrogen to molecules before the density reaches 10^{12} cm^{-3} . After that, the cooling process in the collapsing cloud is dominated by H_2 molecules.

3.2.3. Collapse of the Clouds and Angular Momentum

The angular momentum of a cloud is one of the key factors which influences the radial infall velocity and thermal evolution during the collapse. A cloud with a low angular momentum gravitationally contracts roughly over a free-fall time. Figure 8 shows for our nine representative cases the radial distributions of f_{Kepler} , the ratio of the azimuthal rotation velocity v_{rot} (defined as the variance of the azimuthally averaged velocity perpendicular to the total angular momentum vector inside $M(r)$) to the Keplerian velocity $v_{\text{Kepler}} = \sqrt{GM(r)/r}$.

We see that the profiles of f_{Kepler} are moderately correlated to the thermal evolutions of the clouds, albeit with a large variance at each mass scale $M(r)$. On average, clouds with low temperatures have higher f_{Kepler} (recall that the red, blue, and black lines represent clouds with progressively lower temperatures in this order; see also Figure 7a). Interestingly, Figure 8 also shows that the variance of f_{Kepler} decreases with decreasing enclosed mass $M(r)$ whereas the median value is nearly constant around $\simeq 0.5$ (see also Abel et al. 2002), independent of $M(r)$.

The cloud's degree of rotation also influences the density distribution during the collapse. Figure 9 shows the projected density distributions for 3 clouds with different initial angular momenta. The top panel clearly shows a disk-like structure with notable spiral arms, suggesting that a self-gravitating disk is forming around the protostar. Although the disk-like structure disappears for the lower angular momentum cases, the middle and bottom panels still show a variety of non-spherical structures. This suggests a wide range of dynamics in the gravitational collapse of the primordial clouds. We will revisit

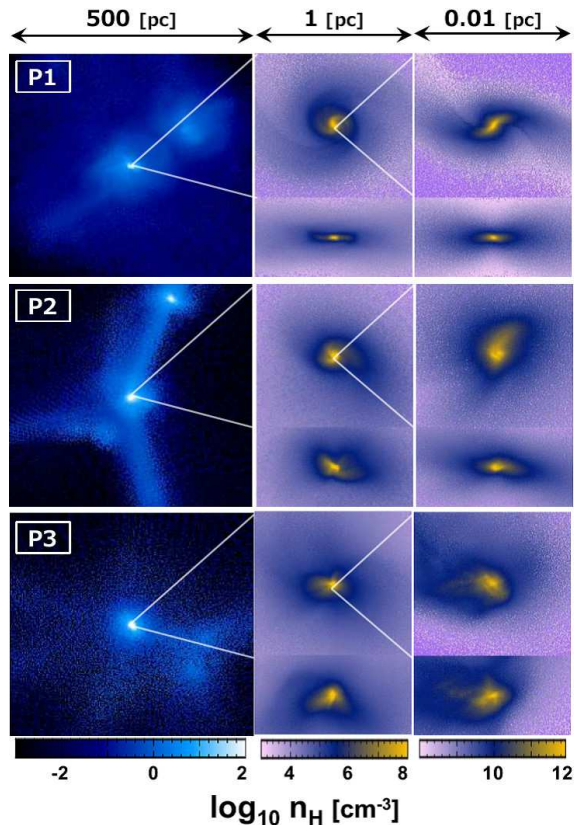


FIG. 9.— Projected gas density distributions for three representative cases at the moment when $n_{\text{H, cen}} = 10^{12} \text{ cm}^{-3}$ (corresponding to those denoted by thick lines in Figure 6), whereby the protostars go through three characteristic evolutionary paths (P1, P2, and P3) in the later accretion phase. The panels show, from left to right, the gas distribution in regions of 500, 1, and 0.01 pc on a side, respectively. We show both the face-on and edge-on views for the 1 pc and 0.01 pc boxes. Note the rotationally supported disk-like structure for the P1 case (top).

this issue in Section 5.1.

3.3. Evolution during the Late Accretion Stage

3.3.1. Mass Accretion Histories and the Final Stellar Masses

We define the late accretion stage as the period during which a protostar gains most of its final mass. Figure 10(a) shows the accretion histories for the entire sample of 110 protostars. The accretion rates gradually decrease with increasing protostellar mass in all the cases. There are, however, substantial variations among the clouds. The accretion rates differ more than a factor of 10 when the stellar masses are only a few solar masses. The protostars’ evolution also differs significantly, reflecting the variation of the mass accretion rates (Figure 10b).

The stellar effective temperature and the UV luminosity rapidly increase when a protostar approaches the ZAMS. At this point UV feedback becomes efficient and ultimately terminates the mass accretion onto the protostar. For high accretion rates, the protostar reaches the ZAMS when the mass is typically larger than one hundred solar masses. In general, the final stellar masses are greater in cases with higher mass accretion rates.

The wide variety of mass accretion profiles are caused by differences in the structure of the gas envelope at the

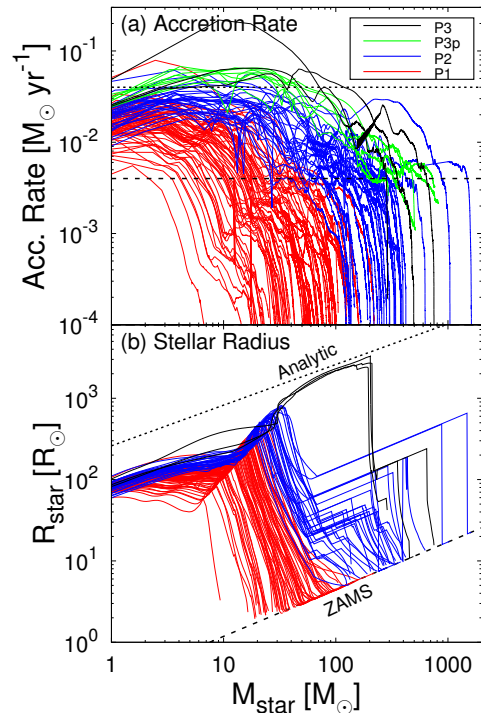


FIG. 10.— Accretion rates (*upper* panel) and stellar radii (*lower* panel) as a function of stellar mass for our entire sample. The colors represent the different paths of the protostellar evolution as in Fig. 6. The two horizontal lines in the *upper* panel are critical values of accretion rates $\dot{M}_{\text{P2}} = 0.004 M_{\odot} \text{ yr}^{-1}$ (dotted; Eq. 5) and $\dot{M}_{\text{P3}} = 0.04 M_{\odot} \text{ yr}^{-1}$ (dashed; Eq. 6). The two diagonal lines in the *lower* panel indicate $260 \times M^{0.5} M_{\odot} \text{ yr}^{-1}$ (dotted; super-giant protostar, Eq. 7) and $0.31 \times M^{0.58} M_{\odot} \text{ yr}^{-1}$ (dashed; ZAMS track derived from the calculation). The green lines in the *top* panel show the results of RHD simulations without the stellar feedback for P3p cases (see also Figure 5) which accurately follow the evolution when the UV radiative feedback is ineffective ($\dot{M} < \dot{M}_{\text{P2}}$).

birth of the protostellar core. Figure 11 shows the radially averaged profiles of the mass accretion rate estimated from the instantaneous density and velocity distributions of the envelope, $4\pi r^2 \rho(r) v_{\text{rad}}(r)$. Note that this is not the accretion history plotted in Fig. 10(a). The “predicted” accretion rates differ quite substantially, being qualitatively consistent with the actual accretion histories found in the radiation hydrodynamic simulations (compare Figs. 10a and 11a). We find that the thermal evolution during the pre-stellar collapse phase plays a key role in shaping the structure of the accreting envelope. Because the thermal evolution depends on the contraction timescale, mechanisms that affect the gravitational collapse such as the cloud’s angular momentum likely affect the overall gas accretion rate. We discuss the origin of the various accretion histories in Section 4.2.

3.3.2. Three Evolutionary Paths of Accreting Protostars

Here we focus on three representative cases characterized by the evolution of the protostellar radius (see Sec. 2.2.1): the KH contracting protostar (P1), the oscillating protostar (P2), and the super-giant protostar (P3). Figure 12 shows the accretion histories for these three selected cases. The accretion rates are highest for P3 and lowest for P1 (see also Sec. 2.2.1). The figure also presents the accretion histories for the same cases

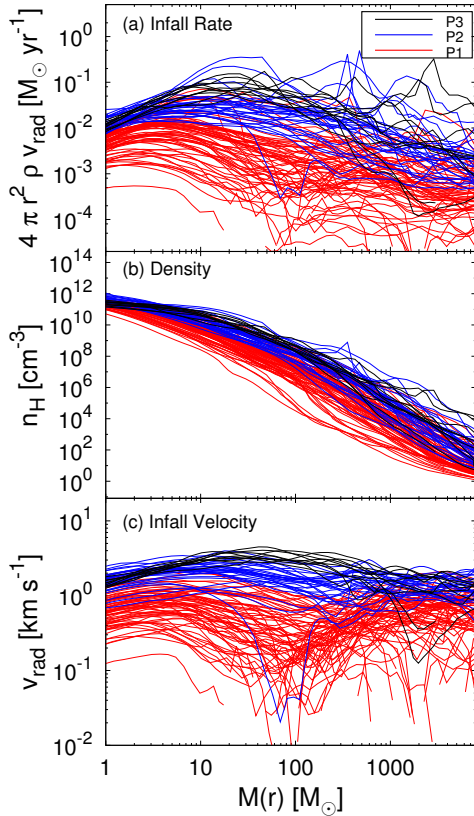


FIG. 11.— The averaged radial distribution of the gas infall rate $4\pi r^2 \rho(r) v_{\text{rad}}(r)$ (top panel), the density (middle) and infall velocity (bottom) profiles when $n_{\text{H, cen}} = 10^{12} \text{ cm}^{-3}$. The colors represent the three paths of the protostellar evolution as in Fig. 6.

but with the UV radiative transfer module switched off, which demonstrates that stellar UV feedback does indeed reduce the accretion rates and the final mass of the protostar late in the evolution.

Case P1 exemplifies the KH contracting protostar studied in Hosokawa et al. (2011, 2012a). The panels (b) - (d) show that, in the adiabatic accretion phase when $M_{\text{star}} \lesssim 10 M_{\odot}$, the effective temperature and ionizing photon (EUV) luminosity is so low that stellar UV feedback is negligible. However, the EUV luminosity rapidly increases once the protostar begins KH contraction at $M_{\text{star}} \simeq 10 M_{\odot}$. As the stellar radius decreases the effective temperature and the EUV luminosity rise. At first, the high accretion rate squelches the HII region (see e.g., Yorke 1986; Omukai & Inutsuka 2002), but eventually the EUV flux is sufficient to ionize the infalling neutral material, driving an expanding bipolar HII region into the accretion envelope (also see Fig. 4). The expanding HII region accelerates the envelope gas outward. At the same time the circumstellar disk is irradiated by the stellar UV, creating a thermally driven disk wind as the disk gradually photo-evaporates. As the accretion rate rapidly decreases, the protostar contracts faster, further increasing the effective surface temperature, and the UV feedback becomes stronger. Figure 12 shows that the final stellar mass for the P1 case is fixed at $\simeq 30 M_{\odot}$, just before the star’s arrival to the ZAMS.

The evolution of P2 looks similar to P1’s before KH contraction ceases at $M_{\text{star}} \simeq 60 M_{\odot}$, when the stel-

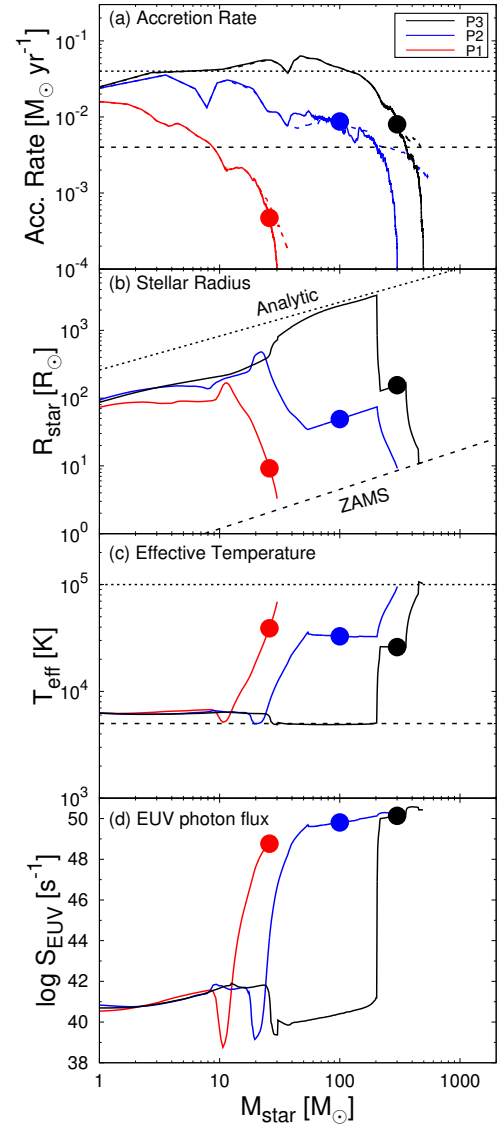


FIG. 12.— The accretion rates (top panel: a) and stellar properties (b, c, and d) versus the stellar mass for the three representative cases of the protostellar evolution. In panel (a), the solid and dashed lines represent the evolution with and without UV radiative feedback from the primordial protostar. The dashed and dotted lines in the panels (a) and (b) are the same as in Fig. 10. Two horizontal lines in panel (c) indicate $T_{\text{eff}} = 10^5 \text{ K}$ (dotted) and 5000 K (dashed). The filled circle marks the epoch when a bipolar HII region first appears in each case.

lar total luminosity reaches the Eddington value. The evolution after this differs from P1’s. The stellar radius begins to increase with increasing mass, entering an oscillating phase⁷. The effective temperature remains almost constant at $\simeq 3 \times 10^4 \text{ K}$ during this phase, and thus the stellar EUV luminosity does not increase. A bipolar HII region first appears late, when the stellar mass reaches $\simeq 100 M_{\odot}$. The oscillating phase is over at $M_{\text{star}} \simeq 200 M_{\odot}$, when the accretion rate falls below the critical rate $\dot{M}_{\text{P2}} = 4 \times 10^{-3} M_{\odot} \text{ yr}^{-1}$ (Eq. 5), al-

⁷ By using our simplified model for P2, the radius does *not* oscillate, see Appendix B.2.

lowing the protostar to resume contraction toward the ZAMS. Mass accretion onto the star is finally halted at $M_{\text{star}} \simeq 300 M_{\odot}$. It is remarkable that, in this case, a large portion of the surrounding gas, $200 M_{\odot}$, is accreted onto the star well after the breakout of the HII region.

The protostar of our representative P3 case enters the super-giant phase soon after the adiabatic accretion phase, when $M_{\text{star}} \simeq 30 M_{\odot}$. The stellar radius monotonically increases with increasing mass, according to the relation (7). The radius exceeds $3000 R_{\odot}$ when the stellar mass is $M_{\text{star}} \simeq 200 M_{\odot}$. The effective temperature is still around 5000 K during this super-giant phase, which means that the EUV luminosity is too low to launch an HII region. The protostar begins to contract after the accretion rate falls below a few $\times 10^{-2} M_{\odot} \text{ yr}^{-1}$, the critical rate given by Eq. (6). The final contraction is very rapid because the KH timescale of the super-giant protostar is very short, less than 10^3 years (e.g., Hosokawa et al. 2012a). Shortly thereafter, KH contraction is interrupted, and the protostellar evolution becomes similar to P2. The HII region begins expanding when the stellar mass is $\simeq 300 M_{\odot}$, which in turn reduces the accretion rate below the critical value \dot{M}_{P2} . As the star contracts once again toward the ZAMS, the stellar UV feedback becomes stronger, and the stellar mass is finally fixed at $M_{\text{star}} \simeq 500 M_{\odot}$.

We note that, in the cases of P2 and P3, the effective temperature of the expanding protostar remains low, which mostly explains why the breakout of the HII region occurs late, when the mass is $\simeq 200$ and $300 M_{\odot}$, respectively. However, Figure 12(d) also shows that the EUV photon luminosity is in fact higher than the case of P1 when the HII region first emerges. This is explained by the fact that the accretion envelope is denser in P2 and P3 because of the higher accretion rates. More ionizing photons are needed to create an HII in dense regions, where hydrogen atoms recombine rapidly (also see Hosokawa et al. 2012b).

4. ORIGIN OF THE WIDE RANGE OF STELLAR MASSES

Our simulations have followed the process of primordial star formation in a number of cosmological halos until the protostars formed reach the ZAMS. We here examine the origin of the wide distribution of stellar masses. First of all, Figure 10 shows a clear correlation between the accretion rates and the final stellar masses. We have already seen that the accretion rate onto a protostar is largely determined by the density and velocity structure of the envelope around the protostar (Fig. 11). We now study in greater detail the formation process of the star-forming gas clouds, whose initial conditions are set at the virialization of the host dark halos.

We shall focus on the overall gas infall rates at two different mass scales; the parent gas cloud and the host dark matter halo. We show that the final stellar masses are indeed correlated with the gas infall rates (Sec. 4.1). We then study how the infall rates are related to other properties of the gas clouds and those of the host halos (Sec. 4.2).

4.1. Stellar Masses and Gas Infall Rates

4.1.1. Infall Rates in Gas Clouds

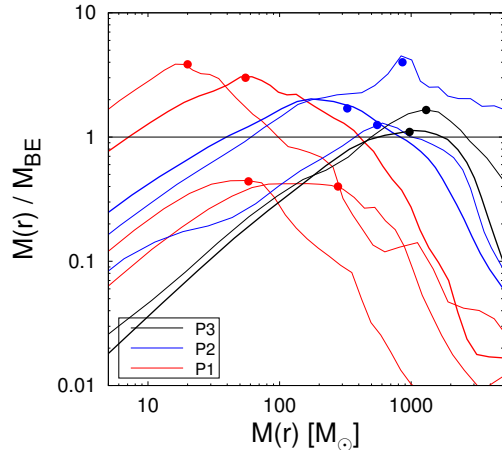


FIG. 13.— The ratio of the enclosed gas mass to the local BE mass for 9 samples when the extremum of $M_{\text{enc}}(r)/M_{\text{BE}}$ reaches the maximum during the collapse. Filled circles mark the positions where $M(r)/M_{\text{BE}}$ takes the maximum, by which we define the cloud mass.

A characteristic mass scale of a gravitationally contracting gas cloud would be the Bonner-Ebert (BE) mass (Bonner 1956; Ebert 1955)

$$M_{\text{BE}} = \frac{1.18 c_s^4}{G^{3/2} P_{\text{ext}}^{1/2}} M_{\odot}, \quad (11)$$

$$\begin{aligned} &\approx 1050 M_{\odot} \cdot \left(\frac{T}{200 \text{ K}} \right)^{3/2} \left(\frac{\mu}{1.22} \right)^{-2} \\ &\cdot \left(\frac{n_{\text{H}}}{10^4 \text{ cm}^{-3}} \right)^{-1/2} \left(\frac{\gamma}{1.66} \right)^2, \quad (12) \end{aligned}$$

where c_s is the sound speed, P_{ext} is the external pressure, n_{H} is the hydrogen number density, μ is the mean molecular weight, and γ is the adiabatic index. A cloud is expected to collapse when the mass within a given radius exceeds the local BE mass, $M_{\text{enc}}(r) > M_{\text{BE}}$. For a primordial gas cloud, this run-away collapse occurs when the first temperature dip appears in the thermal evolutionary track (Fig. 7a), i.e., at the so-called loitering regime (e.g., Bromm et al. 2002). In several of our dark matter halos run-away collapse occurs even though the ratio $M_{\text{enc}}(r)/M_{\text{BE}}$ is (slightly) smaller than unity (Fig. 13). This is because the above BE mass provides a critical mass for gravitational stability only under some idealized conditions, e.g., assuming static motion for the initial condition, which are not realized in our 3D simulations, and the isothermal equation of state. Here, we shall define the mass of the collapsing cloud M_{cloud} to be the mass within a radius at which the ratio of the enclosed mass to the BE mass takes the maximum value during the collapse (see Figure 13). Typically, a primordial gas cloud that cools via H_2 line cooling has a large mass $M_{\text{cloud}} \sim 1000 M_{\odot}$. Note that HD line cooling also operates in some clouds. Such clouds have relatively small masses $M_{\text{cloud}} \sim 10 - 100 M_{\odot}$ when they collapse gravitationally (Section 3.2.2).

In Sec. 3.2, we have seen that the stars formed are more massive for more rapid accretion (Fig. 10), and that the overall accretion rate can be estimated approximately from the density and velocity structure of the

gas envelope at the time when a hydrostatic protostellar core is formed (Fig. 11). Figure 14(a) supports this notion, showing a good correlation between the final stellar masses and the accretion rates estimated from $\dot{M}_{\text{cloud}} = 4\pi r^2 \rho(r) v_{\text{rad}}(r)$ at the cloud mass scale. We evaluate these quantities at radius r_{cloud} within which the enclosed gas mass is M_{cloud} .

Our fitting formula for the correlation

$$M_{\text{popIII}} = 100 M_{\odot} \left(\frac{\dot{M}_{\text{cloud}}}{2.8 \times 10^{-3} M_{\odot} \text{ yr}^{-1}} \right)^{0.8}, \quad (13)$$

is shown in Figure 14(a). Figure 14(b) shows that the deviations from the above relation are indeed small. This relationship should be quite useful, because it allows us to estimate the final stellar mass from \dot{M}_{cloud} without following the detailed protostellar evolution.

4.1.2. Infall Rates at Large Scales

Primordial gas clouds are formed in early dark matter halos, and one can thus expect that some properties of the host dark halos will affect the structure of the gas clouds and possibly the formation of primordial stars within them as well. Figure 14(c) shows that the final stellar masses are indeed correlated with the mass infall rates at the halo scale. We evaluate the density and radial velocity at the virial radius of a halo r_{virial} . Namely, we determine the infall rate from $\dot{M}_{\text{virial}} = 4\pi r_{\text{virial}}^2 \rho(r_{\text{virial}}) v_{\text{rad}}(r_{\text{virial}})$. Similar to Eq. (13), we find a good empirical fit

$$M_{\text{popIII}} = 100 M_{\odot} \left(\frac{\dot{M}_{\text{virial}}}{1.2 \times 10^{-3} M_{\odot} \text{ yr}^{-1}} \right), \quad (14)$$

which indicates that the mass infall rates at the halo scale are roughly proportional to those at the cloud scale. The correlation at the halo scale is somewhat weaker than that at the cloud scale. This is probably because there is a time gap between the virialization of the halos and the onset of collapse. Nonetheless, Equation (14) suggests that the chemo-thermal evolution of the star-forming cloud, the resulting accretion history and the final stellar mass are affected, at least partially, by the very early conditions of the dark matter halos.

4.2. Key Quantities Shaping the Distribution of Final Stellar Masses

We have found a positive correlation between the final stellar masses and the gas infall rates (Fig. 14). This motivates us to further investigate the origin of the diversity of infall rates. To this end we first consider the effects of rotation.

4.2.1. Correlation at the Gas Cloud Scale

To first order the gas mass accretion rate of a Jeans unstable cloud is approximately

$$\dot{M} \sim \frac{M_{\text{Jeans}}}{t_{\text{ff}}} \propto T_{\text{Jeans}}^{1.5}, \quad (15)$$

where $M_{\text{Jeans}} \propto c_s^3 / \rho^{1/2}$ is the Jeans mass and $t_{\text{ff}} = \sqrt{(3\pi)/(32G\rho)} \propto \rho^{-1/2}$ is the free-fall time. Note that the collapsing cloud mass is not strictly equal to the

Jeans mass (M_{BE} ; e.g., Figure 13). Gravitational collapse does not always proceed over a free-fall timescale because rotation can prevent or delay the collapse. The actual *collapse time* t_{cloud} likely depends on the rotation parameter, the ratio of the rotational energy to gravitational energy,

$$\beta_{\text{cloud}} = \frac{\Omega_{\text{cloud}}^2 R_{\text{cloud}}^3}{3GM_{\text{cloud}}}, \quad (16)$$

where $\Omega(r) = |(\vec{r} \times \vec{v}(r))|/r^2 = v_{\perp}(r)/r$ with $v_{\perp}(r)$ at distance r being the velocity perpendicular to the rotational axis. We define Ω_{cloud} at the cloud radius. Naively, we expect that a cloud with a large M_{cloud} and a low β_{cloud} collapses quickly and therefore that the gas accretion rate onto the protostar in the cloud is large (also see Table 3).

Figure 15(a) shows how the final stellar masses depend on the various cloud masses and rotation parameters. As expected, we see that the final stellar mass is higher for larger cloud mass and/or for lower rotation parameter. We find the dependence is approximately

$$M_{\text{popIII}} = 100 M_{\odot} \left(\frac{M_{\text{cloud}}}{350 M_{\odot}} \cdot \frac{0.3}{\beta_{\text{cloud}}} \right)^{0.8}, \quad (17)$$

which also shows the dependences of the infall rates on Eq. (13),

$$\dot{M}_{\text{cloud}} = 2.8 \times 10^{-3} M_{\odot} \text{ yr}^{-1} \left(\frac{M_{\text{cloud}}}{350 M_{\odot}} \cdot \frac{0.3}{\beta_{\text{cloud}}} \right) \quad (18)$$

The relation (17) is plotted for several different stellar masses in Figure 15(a). Whereas Eq. (17) approximately follows the variations of the stellar mass, there are substantial deviations from the fit (Figure 15b).

4.2.2. Correlation at the Dark Halo Scale

We also find that the infall rates at the halo virial radii are correlated with two quantities, the redshift at which a halo forms z_{form} and the mass of the dark halo M_{virial} . Thus the resulting final stellar mass likely depends on these parameters of the host halo. Figure 15(c) shows the final stellar masses for different sets of z_{form} and M_{virial} . We see that massive stars preferentially form at higher redshifts and in more massive dark halos. A good fit providing the estimate for the stellar mass is

$$M_{\text{popIII}} = 100 M_{\odot} \left(\frac{1+z}{20} \right)^3 \left(\frac{M_{\text{virial}}}{3 \times 10^5 M_{\odot}} \right)^2, \quad (19)$$

which with use of Eq. (14) can be converted to

$$\dot{M}_{\text{virial}} = 1.2 \times 10^{-3} M_{\odot} \text{ yr}^{-1} \left(\frac{1+z}{20} \right)^3 \left(\frac{M_{\text{virial}}}{3 \times 10^5 M_{\odot}} \right)^2 \quad (20)$$

Although there is substantial scatter for small cloud masses (Fig. 15d), Eq. (19) provides a reasonable estimate of the final stellar mass using basic properties of the host dark halo.

It is interesting to study why the two parameters M_{virial} and z control the infall rates at the halo virial radius, and why the final stellar masses correlate with the large-scale infall rates. As shown in Sec. 3.2.2 (and in Appendix C), the final stellar mass sensitively depends

TABLE 3
 AVERAGED PROPERTIES FOR THREE EVOLUTION PATHS

Path	\bar{M}_{popIII} (M_{\odot})	\bar{z}_{form}	\bar{M}_{virial} ($10^5 M_{\odot}$)	\bar{M}_{cloud} (M_{\odot})	$\bar{\beta}_{\text{coll}}$
P1	51.2 ± 4.2	18.03 ± 0.55	3.13 ± 0.20	170.5 ± 20.3	0.353 ± 0.017
P2	282.1 ± 30.3	18.86 ± 0.77	4.06 ± 0.35	626.3 ± 80.6	0.298 ± 0.053
P3	483.0 ± 128.3	17.57 ± 0.66	5.06 ± 0.55	837.9 ± 118.9	0.206 ± 0.064

NOTE. — All quantities are the averaged amount for each evolutionary path. Column 2: Final stellar mass, Column 3: Redshift when the central density reaches 10^6 cm^{-3} , Column 4: Mass scale of the virialized dark matter halo, Column 5: Mass scale of the star-forming cloud, and Column 6: The ratio of the rotation to gravitational energy of the cloud.

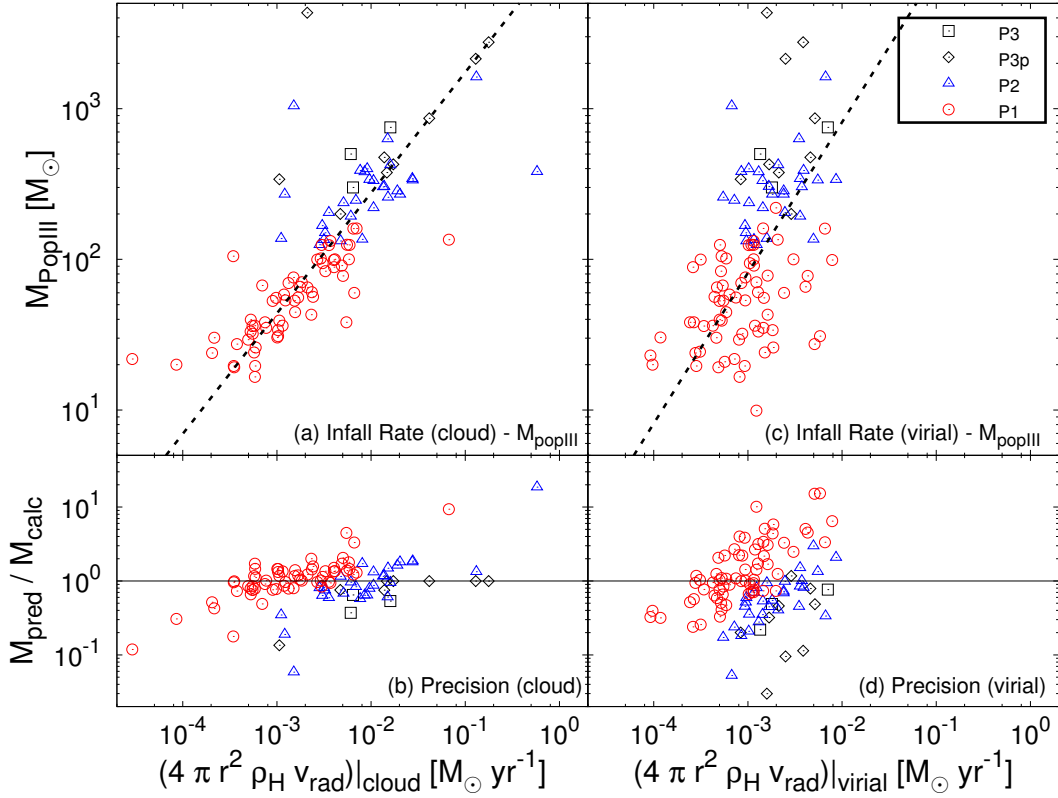


FIG. 14.— Final stellar masses as a function of gas infall rates over cloud scales (*left*) and over dark matter halo scales (*right*). Three colors of symbols represent the evolutionary paths of the protostellar evolution as in Figure 5. The dashed lines represent the fitting functions given by Eqs. (13) and (14). In the bottom frames we plot the ratios of the actual stellar masses to the analytic fitting functions.

on the thermal evolution of a collapsing cloud. Let us suppose that the infall rate is approximately proportional to $M_{\text{virial}}/t_{\text{ff}}$ with some variance due to rotation. Since the mean density within a collapsed halo scales with the mean density of the universe at the epoch z as

$$\rho_{\text{crit}}(z) \equiv \frac{3H^2(z)}{8\pi G}, \frac{H^2(z)}{H_0^2} \simeq \Omega_{\text{m}}(1+z)^3 + \Omega_{\Lambda}, \quad (21)$$

the above estimate should display a dependence $M_{\text{virial}}/t_{\text{ff}} \propto M_{\text{virial}}(1+z)^{3/2}$. This qualitatively explains the overall trend, but we find that the actual dependence on redshift is stronger (Eq. 20).

The additional dependence could be attributed to the

degree of halo spin. Our samples show that on average, at a fixed halo mass, the spin parameter decreases with increasing redshift. At high redshifts, dark matter halos with a given mass are formed from high σ fluctuations of the initial density field. Such halos acquire systematically smaller amounts of angular momentum via tidal interaction with the surrounding structure. The rotational support at the halo scale would be thus inefficient at the higher redshift, which explains the additional dependence on redshift in Eq. (20).

It is worth comparing our findings with the conclusion of previous studies. Gao et al. (2007) present simulations of eight primordial gas clouds. Their gas clouds show significant scatter in the instantaneous mass accretion rate,

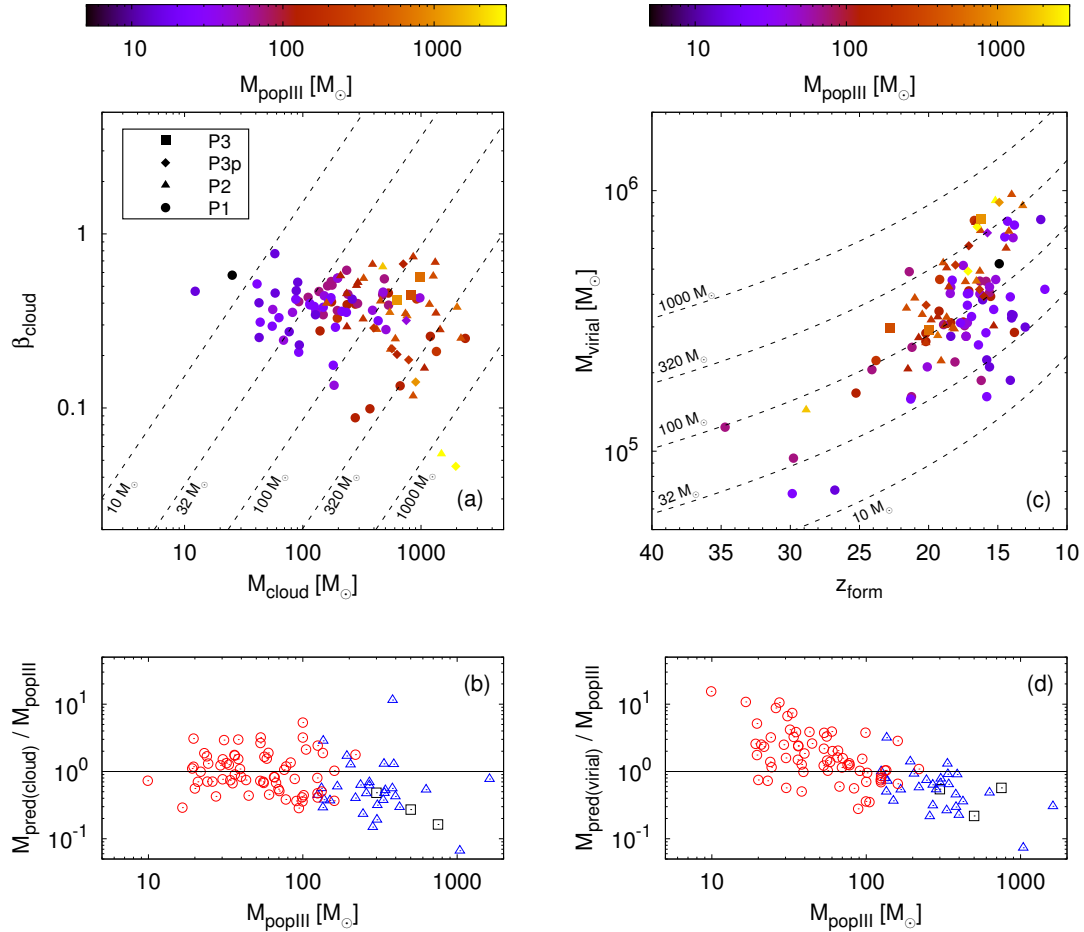


FIG. 15.— *Top*: The rotation parameter β_{cloud} for each of the sample of 110 cloud versus the cloud mass M_{cloud} (left) and the halo mass as a function of the formation redshift z_{form} (right). The different symbols denote the three paths of the protostellar evolution, and the colors are indicative of the final stellar masses (see color scale at the top). The dashed lines represent the fitting functions given by Eqs. (17) and (19) for $M_{\text{popIII}} = 10, 32, 100, 320,$ and $1000 M_{\odot}$. *Bottom*: ratios of estimated masses by Eqs. (17) and (19) to final stellar masses.

over one order of magnitude (see their Figure 11). However, they did not study in detail correlations between the accretion rate and halo mass etc., and thus the origin of scatter among the collapsing clouds remained unclear. It is likely that the scatter is caused by a combination of rotation, halo mass, and the collapse epoch, as we have discussed in this section. O’Shea & Norman (2007) present a statistical study of primordial cloud formation. On the assumption that the stellar mass is proportional to the overall gas infall rate at some initial epoch, they argue that smaller mass stars would form at higher redshifts. This appears inconsistent with our results that $M_{\text{popIII}} \propto (1+z)^3$. O’Shea & Norman (2007) claim that the redshift-dependence of the virial temperature of a halo with a given mass,

$$T_{\text{virial}} \propto M_{\text{virial}}^{2/3} (1+z), \quad (22)$$

is essential for determining accretion rates onto the protostar. In an early stage of primordial cloud formation, H_2 molecules are produced via the H^- channel (Eqs. 8 and 9), which occurs efficiently at higher temperatures. The above dependence of $T_{\text{virial}} \propto (1+z)$ can be under-

stood because slightly more H_2 molecules are formed in a cloud at high redshifts. The resulting temperature of the cloud is lower, and the mass accretion rate onto a protostar would be correspondingly lower because of the relation $\dot{M} \propto T^{-1.5}$. This argument holds for halos with a fixed mass. We have a larger number of halos that have a wide range of M_{virial} . For our cosmological halos that form at different redshifts, the virial temperatures do not simply scale with the collapse redshifts⁸. We actually find an approximately constant $T_{\text{virial}} \simeq 820$ K for collapse. This is reasonable because chemical reactions should take place at the same rate at a constant gas temperature (e.g., Glover 2013). Therefore, if the virial temperature (instead of mass) is fixed, the corresponding halo mass (instead of mass) is lower at higher redshifts, which cancels out the z -dependence in Eq. (22).

⁸ The set of samples in O’Shea & Norman (2007) also shows a large scatter of halo mass in the range of $1.5 \times 10^5 M_{\odot} < M_{\text{virial}} < 7 \times 10^5 M_{\odot}$. However, they suggest that the accretion rates depend only on the collapse redshift. We speculate the apparent discrepancy is seen simply because the statistical set of 12 samples is too small to find the dependence on two variables, $\{z_{\text{virial}}, M_{\text{virial}}\}$.

We note that, whereas the equilibrium H_2 abundance is an increasing function of the temperature, the amount of H_2 molecules necessary to cool the gas is a *decreasing* function of the gas temperature (see Figure 2 in Glover 2013). The balance between the two processes sets the critical temperature above which the gas can cool and condense (Yoshida et al. 2003). Because we select the dark halos where the primordial gas clouds are formed via H_2 cooling, the gas temperatures as well as H_2 abundances do not differ much between members of our sample. Note also that the z -dependence in our relation (19) is attributed to the collapse time rather than the virial temperature, as explained above. Overall, with our large number of gas clouds, we are able to explore a large parameter space such as halo mass and collapse epoch and thus are able to find correlations between multiple quantities.

5. DISCUSSION

5.1. Nature of Dark Matter Halos

The physical properties of the star-forming clouds may depend on the initial angular momentum of the host halo. To study the angular momenta of dark matter and gas, we calculate the spin parameter following the definition of Bullock et al. (2001):

$$\lambda' \equiv \frac{j_{\text{vir}}}{\sqrt{2}R_{\text{vir}}V_{\text{vir}}}, \quad (23)$$

where j_{vir} is the specific angular momentum and $V_{\text{vir}} = \sqrt{GM_{\text{vir}}/R_{\text{vir}}}$ is the circular velocity of the halo. We also compute the angle between the two angular momentum vectors

$$\theta = \cos^{-1} \left[\frac{\mathbf{J}_{\text{DM}} \cdot \mathbf{J}_{\text{gas}}}{|\mathbf{J}_{\text{DM}}||\mathbf{J}_{\text{gas}}|} \right]. \quad (24)$$

Figure 16 shows the range of spin parameters and the alignment angles present in our sample.

We confirm that the distribution of the spin parameters can be fitted by a lognormal distribution (dotted lines in Figure 16)

$$p(\lambda)d\lambda = \frac{1}{\sqrt{2\pi}\sigma_\lambda} \exp \left[-\frac{\ln^2(\lambda/\bar{\lambda})}{2\sigma_\lambda^2} \right] \frac{d\lambda}{\lambda}, \quad (25)$$

with $\bar{\lambda}_{\text{DM}} = 0.0495$, $\sigma_{\lambda_{\text{DM}}} = 0.545$ for the dark matter whereas $\bar{\lambda}_{\text{gas}} = 0.0498$, $\sigma_{\lambda_{\text{gas}}} = 0.750$ for the baryon. The mean angle between the two angular momentum vectors is $\theta_{\text{ave}} \sim 28.2^\circ$ and the median is $\theta_{\text{med}} \sim 19.1^\circ$.

Recently, de Souza et al. (2013) developed an analytic model assuming a tight correlation between the stellar mass and the spin parameter of the host halo. They argue that the mass distribution of the first stars would be shaped by the angular momentum distribution of the host halos that is well described by a log-normal function. We have discussed in section 4 that rotational support delays or possibly prevents cloud collapse and effectively reduces the accretion rate onto the central protostar. Our results, however, show a weaker correlation between the spin parameter and the final stellar mass (see Fig. 17) than the dependence on the other two parameters, z_{form} and M_{virial} . de Souza et al. (2013) use the semi-analytic model of McKee & Tan (2008) to cal-

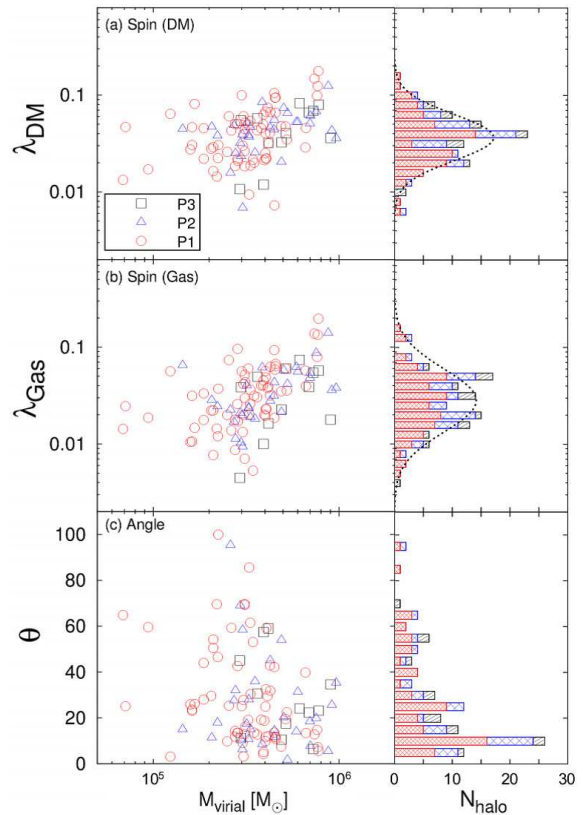


FIG. 16.— Distributions of spin parameters for dark matter (*top* panels) and for gas (*middle*) inside virialized dark matter halos. The *bottom* panel shows the angles between the angular momentum vectors of these two components. In each panel, the *right* frame shows the projected histograms summed over all masses. The dotted lines show best-fit lognormal distributions (Eq. 25) with $\bar{\lambda}_{\text{DM}} = 0.0495$, $\sigma_{\lambda_{\text{DM}}} = 0.545$ for dark matter and $\bar{\lambda}_{\text{gas}} = 0.0498$, $\sigma_{\lambda_{\text{gas}}} = 0.750$ for gas.

culate the stellar mass starting from the angular momentum of the host halos. It is important to point out that McKee & Tan (2008) use f_{Kepler} of a gas cloud, rather than that of a halo, in their accretion model. Although the parent gas cloud properties almost directly affect the pre-stellar collapse, it is less clear how the spin of dark halos affect the *small-scale* processes. Indeed we find no clear trend and thus the stellar mass cannot be estimated from the host halo spin.

5.2. Varieties of Sub-structure of Star-forming Clouds

The variety of mass accretion histories and hence the final stellar masses likely originate from different initial conditions during formation of gas clouds. We have already shown that the overall shapes and structures of collapsing gas clouds reflect different initial conditions. With more than one hundred sample members in our simulations, we find a few cases which show very different properties. In the following we discuss these clouds in greater detail.

5.2.1. The Most Rapidly and the Most Slowly Rotating Clouds

Rotation of a cloud plays a critical role in determining the thermal evolution during the pre-stellar collapse. Figure 18 presents the density distributions at multiple

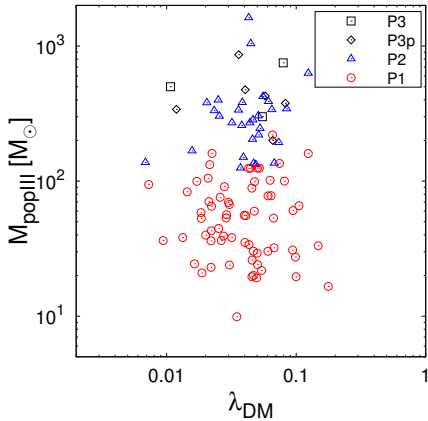


FIG. 17.— The final stellar masses are plotted versus spin parameters of the parent dark matter halos to demonstrate the degree of correlation between the two quantities.

TABLE 4
CLOUD’S PROPERTIES OF TWO EXCEPTIONAL CASES

Case	M_{popIII} (M_{\odot})	z_{form}	M_{virial} ($10^5 M_{\odot}$)	M_{cloud} (M_{\odot})	β_{cloud}
Rapid	9.9	14.90	5.24	25	0.579
Slow	105.0	13.80	2.86	278	0.088

NOTE. — Each column header has the same meaning as in Table 3.

epochs for the two extreme cases of very rapidly and very slowly rotating clouds (*top* and *bottom* panels; Table 4 shows their properties). With fast rotation, the cloud has a disk-like structure that is nearly rotationally supported. Interestingly, this particular cloud is prominent also in the other figures; it shows the lowest temperature evolution track in Figure 7 and the slowest accretion history in Figure 10. The cloud collapses slowly because of rotational support, and cools down to $\simeq 50$ K, almost reaching the CMB temperature floor at $T_{\text{CMB}} \sim 2.73(1+z)$ K. The resulting final stellar mass is only $9.9 M_{\odot}$, which is the smallest among our samples.

The opposite limiting case of the most slowly rotating cloud is presented in the lower panels of Figure 18. The cloud shows little indication of a flattened structure and almost no difference between the face-on and edge-on views. This case corresponds to the case with the lowest value of f_{Kepler} plotted in Figure 8. It has $f_{\text{Kepler}} \simeq 0.2$, less than half of the average. Without strong rotational support, the cloud quickly collapses and the gas mass accretion rate onto the central protostar is large, yielding the final mass of $\simeq 100 M_{\odot}$ (The slowest rotating cloud does not form the most massive star because the protostellar evolution depends also on the cloud mass at the onset of collapse, M_{cloud} ; see Figure 15a in Section 4.2). Clearly, nearly spherical accretion is a favored condition for the formation of very massive primordial stars.

5.2.2. Multiple Density Peaks

Some of our samples show the formation of multiple density peaks in and around a single gas cloud. We have already seen their signatures in Figure 6 as humps in the radial density profiles. We find seven close density

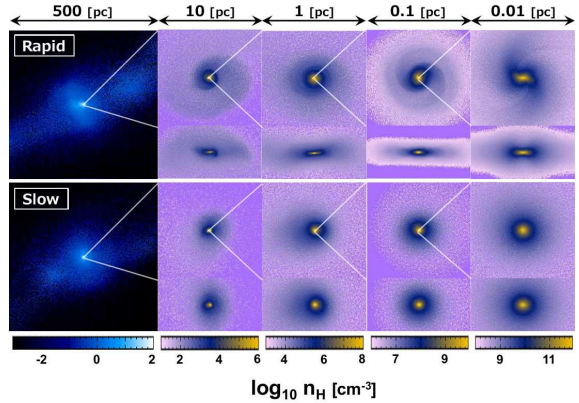


FIG. 18.— Projected gas density distributions when the central density reaches 10^{12} cm^{-3} for two extreme cases: the most rapidly (*top*) and the most slowly (*bottom*) rotating clouds. The physical properties of these clouds are summarized in Table 4.

peaks in six clouds. Figure 19 shows the projected gas density distributions around them. Note that “Frag5” has two neighboring clumps. Several properties of the neighboring gas clumps are summarized in Table 4. The clumps are located at distances $0.05 \sim 2$ pc from the central collapsing core. Note that we only follow the protostellar evolution of the central core. The clumps in the surrounding are smeared out in the subsequent 2D radiation hydrodynamic simulations by averaging the physical quantities over the azimuthal direction. Therefore, whether or not stars can be formed in the neighboring clouds remains unclear in our calculations. Fully three dimensional calculations of protostellar evolution are necessary to determine the final stellar mass(es) for these cases.

We mention that the cosmological simulation of Turk et al. (2009) also show two fragments forming with a 800 AU separation during the run-away collapse of a cloud. We find similar multiple clumps but with even wider separations, though only in a handful of cases out of our sample of 110 clouds. Note also that the clump formation is different from those seen in a self-gravitating circumstellar disk (e.g., Stacy & Bromm 2013, and also see the next section), which produce small separation (< 1000 AU) multiple protostellar systems. Recently, Greif et al. (2013) show the possibility of the chemothermal instability which makes fragments on a scale of a few tens of au.

5.3. Accretion Disk Fragmentation

Recently, Clark et al. (2011) and Greif et al. (2011) studied the evolution of primordial protostellar disks over one hundred years using sink particle techniques. In their simulations, multiple protostars are formed in a disk via gravitational instability. Although our two-dimensional calculations cannot follow the evolution of multiple protostars in a disk, it is worth discussing the possible effect and outcome in such cases.

If disk fragmentation occurs during the mass accretion phase, there are two mechanisms that can reduce the final stellar mass of the central main protostar. One is the reduction of the total gas mass that can be accreted onto the central star, simply because additional sinks are present (fragmentation-induced starvation; i.e.,

TABLE 5
 PROPERTIES OF SEVEN GAS CLUMPS

No.	R (pc)	$M(< R/2)$ (M_\odot)	$\rho_{\text{cen,frag}}$ (cm^{-3})	$t_{\text{ff,frag}}$ (year)	$M_{\text{popIII,prim}}$ (M_\odot)
1	0.05	170	1.48×10^{10}	436	380.3
2	0.08	50	1.92×10^8	3820	53.2
3	0.10	170	2.58×10^8	3300	381.3
4	0.20	120	2.30×10^7	11100	340.0
5a	0.60	270	6.59×10^7	6530	27.4
5b	1.50	900	3.57×10^5	88700	27.4
6	2.00	1300	7.20×10^5	62500	55.5

NOTE. — Column 2: Distance between the primary star and the clump, Column 3: Enclosed mass within $R/2$, Column 4: Central density of the clump, Column 5: Estimated free-fall time, and Column 6: The final stellar mass of the primary star.

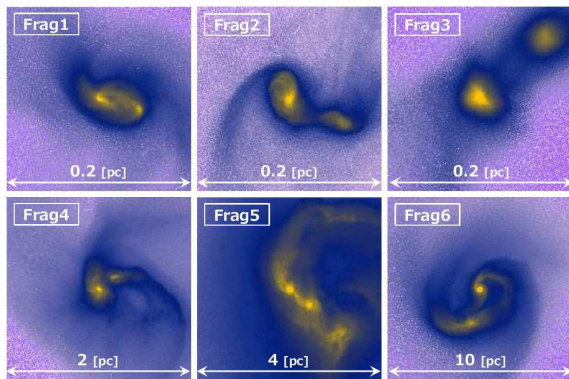


FIG. 19.— Projected gas density distributions for six clouds which have multiple density peaks when the central density reaches 10^{12} cm^{-3} . The clump properties are summarized in Table 4.

Peters et al. 2010). The other is that the structure and evolution of the protostar itself are affected by the reduced accretion rate in a complicated nonlinear way, as we have discussed in the previous sections. With a lower accretion rate, the protostar begins KH-contraction at a lower stellar mass so that the mass accretion is halted by UV radiative feedback in accordance to our P1 evolution. We expect that both of these effects will reduce the final mass of the central protostar.

There is another physical process that we have not included. Primordial magnetic fields are generally considered to be much weaker than in the present-day star-forming cloud, and thus their effects are often ignored in the study of primordial star formation. However, as shown by Machida et al. (2010), even *pico-gauss* magnetic fields are sufficient to transfer angular momentum in the accretion flow via magnetic braking. The accretion disk disappears in cases with a weak magnetic field, and the surrounding gas is accreted onto the protostar directly in a roughly spherical manner. More recently, Turk et al. (2012) and Sur et al. (2012) perform magneto-hydrodynamic simulations of primordial star formation. They show that turbulent velocity fluctuations resolved in their simulations can amplify the magnetic field via the dynamo effect. They argue that magnetic fields can influence the formation and the structure of the accretion disk. Further studies on the effects of magnetic fields are needed to determine the overall

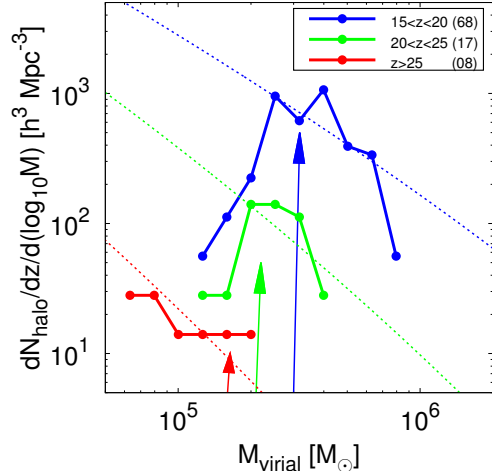


FIG. 20.— Mass functions of the dark halos from our simulations (solid lines). The dotted lines represent the analytic mass functions calculated with the public code developed by Reed et al. (2007). Different colors represent the different formation redshifts. Note that the solid lines have been shifted vertically for comparison. The arrows show the characteristic halo masses collapsing at redshift 17.5 (blue), 22.5 (green), and 27.5 (red), respectively (using Eq. 26 in Barkana & Loeb 2001, for $T_{\text{vir}} \sim 800 \text{ K}$).

impact on the characteristic masses of the first stars.

5.4. Distribution of Stellar Masses

Our study shows a wide mass range for the first generation of stars (Figure 5), including several very massive stars with $M_{\text{popIII}} > 300 M_\odot$. However, the sample should not be regarded as a complete set, because our halo selection is somewhat arbitrary, and the total simulation volume is still too small to be representative of a *cosmological* volume. In this section, we first examine if and how our halo selection is biased and then discuss the fate of the first stars.

5.4.1. Sampling Bias

We use a zoom-in technique to achieve extremely high resolution in large simulation-boxes of $L_{\text{box}} = 1$ and $2 \text{ h}^{-1} \text{ Mpc}$. Although we choose many halos, other (unselected) halos are present that can possibly host first stars. Also, the largest volume of our simulations is $(2 \text{ h}^{-1} \text{ Mpc})^3$. We still miss very rare objects which should exist in a much larger (by a factor $\sim 10^8$) *cosmological* volume of $(1 \text{ h}^{-1} \text{ Gpc})^3$. The earliest forming halo in our sample is located at $z \sim 35$, whereas the very first star in the observable volume is expected to form at $z \rightarrow 50$ (Gao et al. 2007; Naoz & Barkana 2005).

We calculate the mass function of our sample dark matter halos that host primordial stars, and compare it to the Press-Schechter mass function. Figure 20 compares the halo mass functions $dN_{\text{halo}}/dz/d(\log_{10} M)$ at different redshifts. Note that we are concerned with only the overall shape of the mass functions because, with our small, $\sim \text{Mpc}$ volume, the absolute abundance of first star hosts cannot be evaluated robustly. Thus, the amplitudes are shifted arbitrarily for comparison. Three dotted lines in Figure 20 are the Press-Schechter mass functions calculated by the public code of Reed et al.

TABLE 4
FINAL FATE OF POP III STARS

Case	$M_{\text{ZAMS}} (M_{\odot})^1$ (non-rotating)	N_{sample}	$M_{\text{ZAMS}} (M_{\odot})^1$ ($f_{\text{Kepler,ZAMS}} = 0.5$)	N_{sample}
NS	$8 < M < 25$	12	$8 < M < 25$	12
BH	$25 < M < 80$	36	$25 < M < 65$	28
PPISN	$80 < M < 120$	10	$65 < M < 90$	10
PISN	$120 < M < 240$	21	$90 < M < 200$	24
BH	$240 < M$	31	$200 < M$	36

NOTE. — Column 1: final fate of stellar evolution (neutron star (NS), black hole (BH), pulsation pair-instability supernovae (PPISN), and pair-instability supernovae (PISN)), Column 2 and 4: stellar mass range at ZAMS, and Column 3 and 5: number in our sample. Column 2 and 3 are for the non-rotating star, whereas column 4 and 5 are for the highly rotating star.

REFERENCES. — (1) From Figure 12 in Yoon et al. 2012.

(2007). The lower cut-off of the solid lines are a physical effect, reflecting the critical collapse mass at the respective redshift. Note that this is not the resolution limit; the DM particle mass is $< 20 M_{\odot}$ and thus the effective mass resolution is much lower than the cut-off at $\sim 10^4 M_{\odot}$, which is resolved by more than 5000 N-body particles. Overall, the mass function of our sample halos represents the high-mass end and is roughly consistent with the underlying true mass function. Considering the dependence of the final stellar mass on collapse redshift and halo mass, we conclude that the derived stellar mass distribution is not significantly biased.

5.4.2. Final Fate of the First Stars

The main result of our calculated mass distribution indicates that the first stars will end their lives in a variety of ways. Table 4 lists the final fate of zero-metallicity stars calculated by Yoon et al. (2012). There are two sets for different rotational degrees $f_{\text{Kepler}} = 0$ (non-rotating) and 0.5 (rapid-rotating). The corresponding fate for different initial stellar mass ranges are given there. In the table, N_{sample} is the number of stars in the respective mass range found in our simulations. A large fraction of them (about 60%) leave massive black-holes (BH), whereas 11% become neutron stars (remnant of CCSN) and 20% die as pair-instability supernovae regardless of the rotational degrees. We note that there are basically two channels for the Pop III stars to disperse the first heavy elements synthesized in them; core-collapse supernovae and pair-instability supernovae, which leave different characteristic elemental yields.

No clear signature of PISNe is found so far observationally. Although we see a slight deficit in the PISN mass range (Fig. 5), the obtained mass distribution is sufficiently broad that a significant number of PISN very likely occurred in the early universe. Thus, it is necessary to explain the apparent paucity of the PISN signatures in, for example, the elemental abundance patterns of Galactic metal-poor stars. First, there could be some caveat in our calculations, such as our two-dimensional treatment of accretion, which precludes fragmentation of the accretion disks. Our selection of halos to investigate may miss a large number of lower mass halos and/or so-called Pop III.2 stars (see below). Second, there may

be possible biases in observations. The current survey of metal-poor stars are targeted halo stars, whereas most of the remnants of the first stars could be concentrated toward the central regions of the Galaxy (White & Springel 2000; Tumlinson 2010). PISNe can enrich the surrounding gas promptly to a large metallicity, and thus surveys of metal-poor stars might actually miss the stars with PISN signatures (Karlsson et al. 2008, 2013).

In the present paper, we have only considered the so-called Pop III.1 stars, for which the initial conditions are completely determined cosmologically. There are other populations of primordial stars, called Pop III.2 stars, which are formed in a primordial gas that has been affected by the prior existence of other stars (both the Pop III and Pop II stars; the latter can contribute orders of magnitude more strongly, in particular, at low redshifts, $z < 15$, as shown in Figure 6 of Agarwal et al. 2012). These additional populations are characterized by the differences of physical conditions where they are formed, for example inside HII regions (Pop III.2_{ION}) and inside photo-dissociation regions (Pop III.2_{DIS}). Pop III.2 stars are thought to have lower masses on the average than Pop III.1 stars (Yoshida et al. 2007; Hosokawa et al. 2012b). Determining the primordial stellar IMF must necessarily involve all of these cases in a fully cosmological context. It is however beyond the scope of the present paper.

6. CONCLUSION

To study the mass distribution of the first stars, we have performed more than hundred simulations of first star formation in a proper cosmological context. The resulting stellar masses range from $M_{\text{popIII}} \sim 10$ to $1000 M_{\odot}$. Most of them are distributed around a few tens to a few hundreds solar masses. A number of the first stars would end their lives leaving massive BHs, and a significant fraction of stars die as supernovae. We summarize our main results as follows.

1. The collapse time-scale is the key quantity that determines the thermal evolution of the gas clouds. Rapidly collapsing clouds follow the well-known evolution path which is controlled by H_2 cooling. Slowly collapsing clouds cool efficiently because of the less effective compressional heating and the longer time scale for the coolants to be produced. When the temperature decreases to ~ 100 Kelvin, HD molecules are formed efficiently, and the additional HD molecular cooling further lowers the temperature to the CMB temperature. The physical structure of the gas envelope around a protostellar core also differs among our sample of clouds, reflecting the different thermal evolution during the collapse. This in turn leads to different accretion histories onto the protostars as seen in the subsequent evolutionary stage.
2. The main self-regulation mechanism of protostellar growth is UV feedback; the resulting stellar mass differs considerably among our sample. On average, the final stellar mass is larger for more rapid mass accretion. Protostars approach the ZAMS at larger stellar masses in such cases. Interestingly, in cases with very rapid accretion $\dot{M} \gtrsim 4 \times 10^{-3} M_{\odot} \text{ yr}^{-1}$, the protostar greatly

expands so that the stellar effective temperature remains below 10^4 K. The ionizing photon luminosity remains so low that UV feedback never becomes strong enough to prevent mass accretion (e.g., Hosokawa et al. 2012a). We argue that rapid mass accretion is a promising path for forming very massive ($\gtrsim 10^3 M_\odot$) stars in the early universe (see e.g. Hosokawa et al. 2012a, 2013).

3. The overall accretion rate can be estimated from the structure of the gas envelope around a protostellar core. The structure itself is affected by the thermal evolution during the run-away collapse. We can predict the final stellar mass from the conditions in the early state of the gas cloud formation, and to a less rigorous extent even from the properties of dark matter halos. In fact, we have seen correlations between the final stellar masses and infall rates at the scales of both the gas clouds and the dark matter halos (Eqs. 13 and 14). We have identified key physical quantities that determine the infall rates: the parent cloud mass and the rotation parameter (for the cloud scale), and the formation redshift and the virial mass of the host halo (for the halo scale).

Through these simulations we have found new protostellar evolutionary paths (P2 and P3) that typically lead to the formation of very massive ($>$ a few $100 M_\odot$) first stars. Although this mode of first star formation is not dominant, the relative abundance of the most massive stars is important for the study of the formation of supermassive black holes in the early universe.

We have identified a key feedback mechanism that regulates the mass growth and determines the final mass of a primordial protostar. Because the strength of the radiative feedback is determined by the protostellar evolution itself, accurate modeling of the time-dependent accretion and the resulting protostellar evolution is clearly needed. Statistical studies using 3D radiation hydrodynamic simulations would be one of the next challenges for deriving the initial stellar mass function of the first stars.

We have shown that the final mass of a central star can be estimated reasonably well from a few physical proper-

ties of the host halo. In principle, we can derive the “cosmological” stellar IMF theoretically if we know the mass function of the host dark matter halos and its redshift-evolution, and also the other important quantities such as the gas infall rates. The results can be used, for example, to predict the early chemical evolution and the characteristic signatures of the first galaxies. It is definitely worth developing such a global evolution model using large-scale cosmological simulations.

Future observations will exploit the next-generation facilities such as JWST, 30 - 40 meter telescopes, and radio telescope arrays, to probe the evolution of the high-redshift universe. Data from such observations, combined with detailed studies of the Galactic metal-poor stars, will ultimately constrain the characteristic mass of the first generation of stars.

We are grateful to Sanemichi Z. Takahashi, for discussions on the numerical treatment of angular momentum transport. We also thank Masahiro N. Machida, Hajime Susa, Kenji Hasegawa, Kei Tanaka, and Kohei Inayoshi for stimulating discussions and Thomas H. Greif for helpful comments on this study. The numerical calculations were in part carried out on T2K-Tsukuba System at Center for Computational Sciences, University of Tsukuba, SR16000 at YITP in Kyoto University, and Cray XT4, XC30 and the general-purpose PC farm at Center for Computational Astrophysics, CfCA, of National Astronomical Observatory of Japan. The work is supported in part by the Global COE Program “The Physical Sciences Frontier,” MEXT, Japan (SH), the Grands-in-Aid by the Ministry of Education, Science and Culture of Japan (25800102 TH, 21684007 and 25287040 KO), and a grant from the Hayakawa Satio Fund awarded by the Astronomical Society of Japan. Portions of this work were conducted at the Jet Propulsion Laboratory, California Institute of Technology, operating under a contract with the National Aeronautics and Space Administration (NASA). The page charge of this paper is partly supported by Center for Computational Astrophysics, National Astronomical Observatory of Japan.

REFERENCES

- Abel, T., Bryan, G. L., & Norman, M. L. 2002, *Science*, 295, 93
 Agarwal, B., Khochfar, S., Johnson, J. L., et al. 2012, *MNRAS*, 425, 2854
 Alvarez, M. A., Bromm, V., & Shapiro, P. R. 2006, *ApJ*, 639, 621
 Barkana, R., & Loeb, A. 2001, *Phys. Rep.*, 349, 125
 Barkat, Z., Rakavy, G., & Sack, N. 1967, *Physical Review Letters*, 18, 379
 Bond, J. R., Arnett, W. D., & Carr, B. J. 1984, *ApJ*, 280, 825
 Bonnor, W. B. 1956, *MNRAS*, 116, 351
 Bromm, V., Coppi, P. S., & Larson, R. B. 2002, *ApJ*, 564, 23
 Bromm, V., & Yoshida, N. 2011, *ARA&A*, 49, 373
 Bromm, V., Yoshida, N., Hernquist, L., & McKee, C. F. 2009, *Nature*, 459, 49
 Bullock, J. S., Dekel, A., Kolatt, T. S., et al. 2001, *ApJ*, 555, 240
 Caffau, E., Bonifacio, P., François, P., et al. 2011, *Nature*, 477, 67
 Chiaki, G., Yoshida, N., & Kitayama, T. 2013, *ApJ*, 762, 50
 Clark, P. C., Glover, S. C. O., Smith, R. J., et al. 2011, *Science*, 331, 1040
 de Souza, R. S., Ciardi, B., Maio, U., & Ferrara, A. 2013, *MNRAS*, 428, 2109
 Ebert, R. 1955, *ZAp*, 37, 217
 Frebel, A., Johnson, J. L., & Bromm, V. 2009, *MNRAS*, 392, L50
 Gammie, C. F. 1996, *ApJ*, 457, 355
 Gao, L., Yoshida, N., Abel, T., et al. 2007, *MNRAS*, 378, 449
 Glover, S. 2013, in *Astrophysics and Space Science Library*, Vol. 396, *Astrophysics and Space Science Library*, ed. T. Wiklund, B. Mobasher, & V. Bromm, 103
 Greif, T. H., Bromm, V., Clark, P. C., et al. 2012, *MNRAS*, 424, 399
 Greif, T. H., Springel, V., & Bromm, V. 2013, *ArXiv e-prints*, arXiv:1305.0823
 Greif, T. H., Springel, V., White, S. D. M., et al. 2011, *ApJ*, 737, 75
 Heger, A., & Woosley, S. E. 2002, *ApJ*, 567, 532
 Hirano, S., & Yoshida, N. 2013, *ApJ*, 763, 52
 Hosokawa, T., & Omukai, K. 2009, *ApJ*, 691, 823
 Hosokawa, T., Omukai, K., & Yorke, H. W. 2012a, *ApJ*, 756, 93
 Hosokawa, T., Omukai, K., Yoshida, N., & Yorke, H. W. 2011, *Science*, 334, 1250
 Hosokawa, T., Yorke, H. W., Inayoshi, K., Omukai, K., & Yoshida, N. 2013, *ArXiv e-prints*, arXiv:1308.4457

- Hosokawa, T., Yoshida, N., Omukai, K., & Yorke, H. W. 2012b, *ApJ*, 760, L37
- Johnson, J. L., Dalla, V. C., & Khochfar, S. 2013, *MNRAS*, 428, 1857
- Johnson, J. L., Greif, T. H., & Bromm, V. 2007, *ApJ*, 665, 85
- Karlsson, T., Bromm, V., & Bland-Hawthorn, J. 2013, *Reviews of Modern Physics*, 85, 809
- Karlsson, T., Johnson, J. L., & Bromm, V. 2008, *ApJ*, 679, 6
- Kitsionas, S., & Whitworth, A. P. 2002, *MNRAS*, 330, 129
- Komatsu, E., Smith, K. M., Dunkley, J., et al. 2011, *ApJS*, 192, 18
- Li, Y., Hernquist, L., Robertson, B., et al. 2007, *ApJ*, 665, 187
- Machida, M. N., Omukai, K., & Matsumoto, T. 2010, in *American Institute of Physics Conference Series*, Vol. 1294, American Institute of Physics Conference Series, ed. D. J. Whalen, V. Bromm, & N. Yoshida, 56–61
- Maio, U., Khochfar, S., Johnson, J. L., & Ciardi, B. 2011, *MNRAS*, 414, 1145
- Matsuda, T., Satō, H., & Takeda, H. 1969, *Progress of Theoretical Physics*, 42, 219
- McKee, C. F., & Tan, J. C. 2008, *ApJ*, 681, 771
- Naoz, S., & Barkana, R. 2005, *MNRAS*, 362, 1047
- Ohkubo, T., Nomoto, K., Umeda, H., Yoshida, N., & Tsuruta, S. 2009, *ApJ*, 706, 1184
- Omukai, K. 2000, *ApJ*, 534, 809
- Omukai, K., & Inutsuka, S.-i. 2002, *MNRAS*, 332, 59
- Omukai, K., & Nishi, R. 1998, *ApJ*, 508, 141
- Omukai, K., & Palla, F. 2001, *ApJ*, 561, L55
- , 2003, *ApJ*, 589, 677
- O’Shea, B. W., & Norman, M. L. 2007, *ApJ*, 654, 66
- , 2008, *ApJ*, 673, 14
- Palla, F., Salpeter, E. E., & Stahler, S. W. 1983, *ApJ*, 271, 632
- Peters, T., Klessen, R. S., Mac Low, M.-M., & Banerjee, R. 2010, *ApJ*, 725, 134
- Reed, D. S., Bower, R., Frenk, C. S., Jenkins, A., & Theuns, T. 2007, *MNRAS*, 374, 2
- Ripamonti, E. 2007, *MNRAS*, 376, 709
- Ripamonti, E., Haardt, F., Ferrara, A., & Colpi, M. 2002, *MNRAS*, 334, 401
- Ritter, J. S., Safraneck-Shrader, C., Gnat, O., Milosavljević, M., & Bromm, V. 2012, *ApJ*, 761, 56
- Shakura, N. I., & Sunyaev, R. A. 1973, *A&A*, 24, 337
- Springel, V. 2005, *MNRAS*, 364, 1105
- Stacy, A., & Bromm, V. 2013, *MNRAS*, 433, 1094
- Stacy, A., Greif, T. H., & Bromm, V. 2012, *MNRAS*, 422, 290
- Stahler, S. W., Palla, F., & Salpeter, E. E. 1986, *ApJ*, 302, 590
- Sur, S., Federrath, C., Schleicher, D. R. G., Banerjee, R., & Klessen, R. S. 2012, *MNRAS*, 423, 3148
- Susa, H. 2013, *ApJ*, 773, 185
- Takahashi, S. Z., Inutsuka, S.-i., & Machida, M. N. 2013, *ApJ*, 770, 71
- Toomre, A. 1964, *ApJ*, 139, 1217
- Tumlinson, J. 2010, *ApJ*, 708, 1398
- Tumlinson, J., Venkatesan, A., & Shull, J. M. 2004, *ApJ*, 612, 602
- Turk, M. J., Abel, T., & O’Shea, B. 2009, *Science*, 325, 601
- Turk, M. J., Oishi, J. S., Abel, T., & Bryan, G. L. 2012, *ApJ*, 745, 154
- Umeda, H., & Nomoto, K. 2005, *ApJ*, 619, 427
- Volonteri, M. 2012, *Science*, 337, 544
- White, S. D. M., & Springel, V. 2000, in *The First Stars*, ed. A. Weiss, T. G. Abel, & V. Hill, 327
- Wise, J. H., Turk, M. J., Norman, M. L., & Abel, T. 2012, *ApJ*, 745, 50
- Yoon, S.-C., Dierks, A., & Langer, N. 2012, *A&A*, 542, A113
- Yorke, H. W. 1986, *ARA&A*, 24, 49
- Yorke, H. W., & Bodenheimer, P. 1999, *ApJ*, 525, 330
- Yorke, H. W., & Kaisig, M. 1995, *Computer Physics Communications*, 89, 29
- Yorke, H. W., & Sonnhalter, C. 2002, *ApJ*, 569, 846
- Yoshida, N., Abel, T., Hernquist, L., & Sugiyama, N. 2003, *ApJ*, 592, 645
- Yoshida, N., Oh, S. P., Kitayama, T., & Hernquist, L. 2007, *ApJ*, 663, 687
- Yoshida, N., Omukai, K., & Hernquist, L. 2008, *Science*, 321, 669
- Yoshida, N., Omukai, K., Hernquist, L., & Abel, T. 2006, *ApJ*, 652, 6
- Zhu, Z., Hartmann, L., & Gammie, C. 2010a, *ApJ*, 713, 1143
- Zhu, Z., Hartmann, L., Gammie, C. F., et al. 2010b, *ApJ*, 713, 1134

APPENDIX

ANGULAR MOMENTUM TRANSPORT IN THE ACCRETION DISK

In a rapidly accreting circumstellar disk, angular momentum is transferred outward by torques produced by non-axisymmetric spiral structure. In our previous work (Hosokawa et al. 2011), we adopted the so-called α -viscosity (Shakura & Sunyaev 1973) to mimic this effect in axisymmetric 2D radiation hydrodynamic simulations. The equation of angular momentum transport is written

$$\frac{\partial A}{\partial t} + \nabla \cdot (A\vec{v}) = -\frac{1}{R} \frac{\partial}{\partial R} \left(R^3 \eta \frac{\partial \Omega}{\partial R} \right), \quad (\text{A1})$$

where Ω is angular velocity, $\eta = 2\alpha\rho c_s^2/(3\Omega)$, and α is a dimensionless free parameter. Hosokawa et al. (2011) model the spatial distribution of the alpha-parameter with an analytic function

$$\alpha(R, Z) = \alpha_0 \exp\left(-\frac{Z}{H(R)}\right), \quad (\text{A2})$$

where α_0 is a constant free parameter, and $H(R)$ is the scale height of the circumstellar disk at each radial coordinate R . The fiducial value of α_0 is 0.6 in Hosokawa et al. (2011).

In this paper, we improve the above description with an additional R -dependence of α_0 . Following Zhu et al. (2010a) and Takahashi et al. (2013), we adopt the functional form proposed by Gammie (1996),

$$\alpha_0(R) = \alpha_{\max} e^{-Q(R)^4}, \quad (\text{A3})$$

where $Q(R)$ is the Toomre Q -parameter (Toomre 1964), which measures the gravitational stability of the disk. The underlying idea of the above dependence is as follows. With the small values of $Q < 1$, α_0 approaches α_{\max} because the angular momentum transport should be efficient with spiral arms emerging in such a highly unstable disk. The large α_0 promotes the mass accretion, which reduces the disk surface density and increases Q . On the other hand, α_0 has a cut-off for $Q > 1$, because the spiral arms disappear in a stable disk. Materials falling onto the disk accumulate

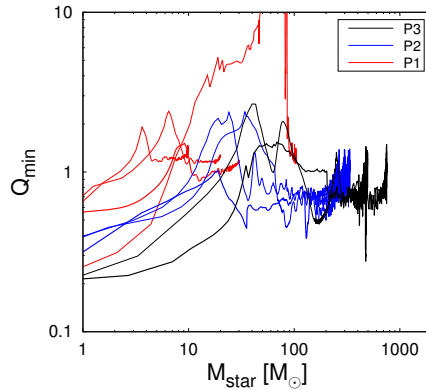


FIG. 21.— Evolution of the minimum Toomre Q -parameter as a function of the stellar mass for the same cases as in Figure 6. We see that Q_{\min} is close to unity, which is generally expected for a self-gravitating circumstellar disk, in almost all the cases. Only one case, for which the cloud rotation is the slowest of the entire sample, shows a very large Q_{\min} (see discussion in text).

without angular momentum transport, which enhances the disk surface density and reduces Q . With the above regulation mechanism, the self-gravitating disk hovers around the marginally stable steady state with $Q \sim 1$.

In this paper, we adopt $\alpha_{\max} = 2$ for all the examined cases. Figure 21 shows the evolution of the minimum Toomre Q -values in several cases. We see that Q_{\min} eventually converges to around unity in each case. Only one case shows a peculiar evolution with Q_{\min} reaching 10 at maximum. This corresponds to the most slowly rotating cloud explained in Sec. 5.2.1. A circumstellar disk hardly forms in this case.

Mass accretion continues smoothly without “ring-like” disk fragmentation of the disk in our simulations. In test calculations with lower values of α_{\max} ring-like fragmentation does occur occasionally with very rapid mass accretion. We avoid this on purpose with our choice of α_{\max} because we cannot treat fragmentation in 2D axisymmetric simulations. We consider our results for very rapid mass accretion a conservative upper limit of the final stellar mass resulting from stellar UV feedback. Disk fragmentation could further reduce the final stellar masses (also see Sec. 5.3).

MODELING PROTOSTELLAR EVOLUTION

As described in Sec. 2.2, our stellar evolution code occasionally has convergence difficulties for the extremely high and highly variable accretion rates encountered in the P2 and P3 scenarios. Whereas for the P1 cases we can use the same method as Hosokawa et al. (2011), we switch to the following simple procedure of protostellar evolution when convergence difficulties arise.

Oscillating Protostar (P2)

The solid line in Figure 22 shows the numerically calculated evolution with the constant accretion rate $\dot{M} = 6 \times 10^{-3} M_{\odot} \text{ yr}^{-1}$. In this case, our stellar evolution code experienced convergence difficulties after the stellar mass exceeded $60 M_{\odot}$, when the radius began to increase and the total luminosity reached the Eddington limit (also see Sec. 2.2.1). The problem worsened when we used the time-dependent mass accretion histories obtained in the simulations.

We adopt the following simplified procedure instead. First, we numerically calculate the protostellar evolution until the protostar begins to oscillate. After that, we analytically model the evolution of the stellar radius and luminosity using the same power-law functions as for non-accreting ZAMS stars,

$$R(M_*) = R_{\text{edd}} \left(\frac{M_*}{M_{\text{edd}}} \right)^{0.58} R_{\odot}, \quad (\text{B1})$$

$$L(M_*) = L_{\text{edd}} \left(\frac{M_*}{M_{\text{edd}}} \right)^{1.30} L_{\odot}, \quad (\text{B2})$$

where M_{edd} , R_{edd} , and L_{edd} are the stellar quantities when the star begins to oscillate. Once the accretion rate drops below the critical value $4 \times 10^{-3} M_{\odot} \text{ yr}^{-1}$ (Eq. 5), we let the star to contract over the KH timescale according to

$$R(M_*) = R_{\text{prev}} + dt \cdot (R(M_*)_{\text{ZAMS}} - R_{\text{prev}}) / t_{\text{KH}} R_{\odot}, \quad (\text{B3})$$

$$L(M_*) = L_{\text{prev}} + dt \cdot (L(M_*)_{\text{ZAMS}} - L_{\text{prev}}) / t_{\text{KH}} L_{\odot}, \quad (\text{B4})$$

where R_{prev} and L_{prev} are the stellar quantities at the previous step of calculation, and

$$R(M_*)_{\text{ZAMS}} = 3.109 \times 10^{-1} \left(\frac{M_*}{M_{\text{edd}}} \right)^{0.58} R_{\odot}, \quad (\text{B5})$$

$$L(M_*)_{\text{ZAMS}} = 3.939 \times 10^3 \left(\frac{M_*}{M_{\text{edd}}} \right)^{1.30} L_{\odot}. \quad (\text{B6})$$

After the star reaches the ZAMS stage, the radius and luminosity are assumed to be the same as those of non-accreting ZAMS stars.

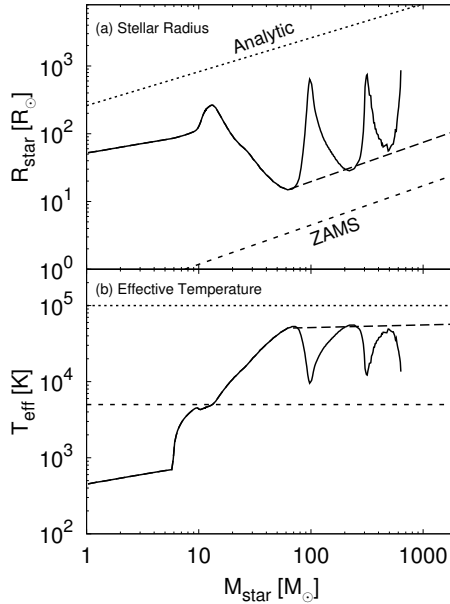


FIG. 22.— Our analytic model for the evolutionary path P2 of an accreting protostar (long-dashed lines). The top and bottom panels show the evolution of the stellar radius and effective temperature with increasing the stellar mass. The solid lines show the numerical results for $\dot{M} = 6 \times 10^{-3} M_{\odot} \text{ yr}^{-1}$ taken from Hosokawa et al. (2012a). The dotted and short-dashed lines are the same as in Figures 12(b) and (c).

Super-Giant Protostar (P3)

The convergence difficulties described above worsen when considering P3 evolution. In this case we first perform the 2D RHD simulation without stellar UV feedback and record the mass accretion history without calculating stellar evolution. Next, we numerically calculate stellar evolution as a post process from the accretion history. We record the stellar evolution track until the stellar total luminosity reaches the Eddington value. We repeat the RHD simulation and include UV feedback using the recorded stellar evolution track. Finally, we switch to the same analytic model as for the path P2 for the evolution beyond the recorded stellar evolution track. We find that UV feedback significantly affects the accretion only after the protostar enters the evolutionary path P2.

It would be very time-consuming to use the procedure described above for all twelve cases of P3 evolution. Instead, we have used this procedure for only three cases. For the other nine cases, we estimate the final stellar masses using the relation (17). We designate these nine cases as the path P3p in the captions of Figures 5 and 10.

DEPENDENCE OF THERMAL EVOLUTION ON THE COLLAPSING TIMESCALE

As described in Sec. 3.2.2, HD line cooling, which has been thought to be unimportant in Pop III.1 star formation, is actually quite effective during the early run-away collapse stage in several of our cases. We argue that HD molecules form when rotational support of the cloud can sufficiently slow the collapse. Here we test this hypothesis using a simple one-zone model, which follows the thermal evolution at the center of the collapsing cloud (e.g., Omukai 2000; Chiaki et al. 2013). Figure 23 shows the results for different collapsing timescales, $t_{\text{coll}} = f \cdot t_{\text{ff}}$, with $f = 0.6, 1.0, 1.8, 3.2, 5.6,$ and 10.0 (solid lines). Several examples of the thermal evolution obtained in the 3D hydrodynamic simulations (colored dashed lines with filled circles) are also plotted in this figure. Our one-zone results can well explain the wide variety of thermal evolution. We briefly describe the essence of the evolution in each density range below.

Low Density ($n_{\text{H, cen}} < 10^8 \text{ cm}^{-3}$)—

In this stage, HD cooling could significantly affect the thermal evolution for the slowly collapsing cloud. HD cooling becomes efficient when the gas temperature falls below 100 K. The additional coolant HD further reduces the temperature to the cosmological temperature floor, T_{CMB} . Figure 23 shows that the gas temperature falls more strongly for the longer collapse timescale. The gas temperature falls below 100 K via H_2 and HD cooling when $f > 1.8$. Indeed, this critical value of f can be analytically derived by requiring the collapse timescale $t_{\text{coll}} = f \cdot t_{\text{ff}}$ to be equal to the H_2 cooling time at $T = 100 \text{ K}$ (and $n_{\text{H}} = 10^3 \text{ cm}^{-3}$). The resulting value of $f_{\text{crit}} = 1.2$ is close to the numerical result.

Intermediate Density ($10^8 \text{ cm}^{-3} < n_{\text{H, cen}} < 10^{12} \text{ cm}^{-3}$)—

At densities above 10^8 cm^{-3} the three-body H_2 formation reaction becomes quite efficient, and H_2 formation heating becomes more important than heating by compression. Nevertheless, the equilibrium temperature is lower for cases with a higher abundance of hydrogen molecules. The middle panel of Figure 23 shows that the more slowly collapsing clouds have a higher H_2 fraction at densities $10^8 \text{ cm}^{-3} < n_{\text{H, cen}} < 10^{12} \text{ cm}^{-3}$, because more H_2 is formed when the collapse time is longer. H_2 cooling dominates the cooling, so the temperature is lower with the larger f in this density

range.

High Density ($n_{\text{H, cen}} > 10^{12} \text{ cm}^{-3}$)—

At these high densities all of the hydrogen has been converted into its molecular form. Compression heating, which increases with decreasing collapse timescale, becomes the dominant heating process. The heating rate is thus lower for the longer collapse timescale. This explains why the temperature remains lower with the larger f in the highest density range.

— Figure 24 shows the correlation between f and the final stellar masses in our numerical results. f is evaluated in the following manner. We calculate the timescale between two snapshots during which the central density decouples, $n_{\text{cen}} \rightarrow 10 \times n_{\text{cen}}$. f is the ratio of this collapsing timescale, t_{coll} , to the free-fall time,

$$t_{\text{ff}} = \left(\frac{3\pi}{32G\rho} \right)^{1/2}. \quad (\text{C1})$$

We average these ratios at $n_{\text{cen}} = 10^4$ to 10^{12} cm^{-3} and assume it as the characteristic parameter of the collapsing cloud, f . The good correlation presented here suggests that the thermal evolution in our 3D cosmological simulations really depends on the parameter f .

McKee & Tan (2008) adopt the rotational degree of the cloud f_{Kepler} as a key parameter which determines the final stellar mass in their semi-analytic model. However, they only consider that the rotational support of the cloud slows down the mass accretion onto the star. We have shown that the rotational support reduces the accretion rate by changing the chemo-thermal evolution as well as the gas dynamics.

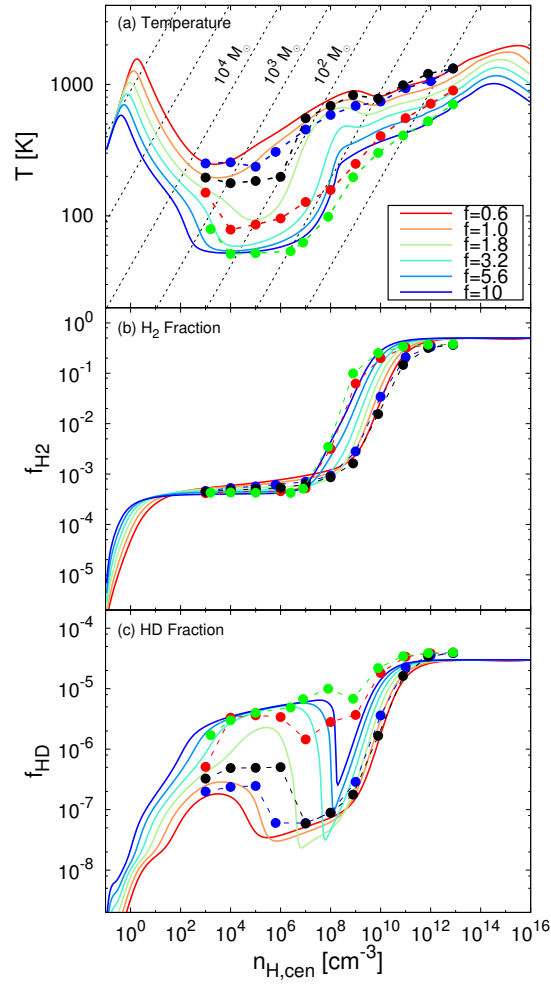


FIG. 23.— Comparison of the thermal evolution during the cloud collapse between the simulation results (dashed lines and filled circles) and one-zone models (solid lines). The solid lines with the different colors represent the different collapse timescales, $t_{\text{coll}} = f \cdot t_{\text{ff}}$, with $f = 0.6, 1.0, 1.8, 3.2, 5.6, 10$, which is a parameter for one-zone modeling. The red, blue, and black dashed lines represent the same 3D simulation cases shown in Figure 9, whereas the green line is for the most rapidly rotating cloud shown in Figure 18. The black dashed lines in the top panel present $\rho - T$ relations for given values of the Jeans mass.

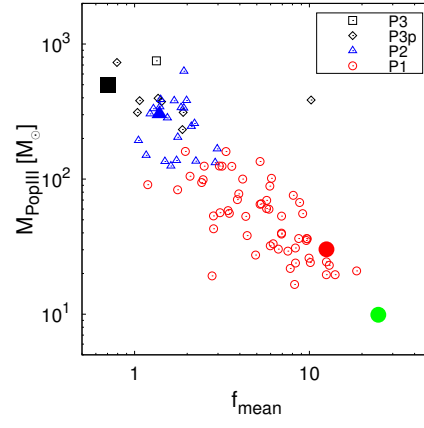


FIG. 24.— Correlation between the ratio $f = t/t_{\text{ff}}$ of the averaged relative collapse timescale to the free-fall timescale and the final stellar masses in our numerical simulations. The different symbols denote the different paths of the protostellar evolution as in Figure 14.